International Journal of Pharmaceutics 423 (2012) 264–280

Contents lists available at SciVerse ScienceDirect

International Journal of Pharmaceutics

journal homepage: www.elsevier.com/locate/ijpharm

Computational fluid dynamics (CFD) insights into agitation stress methods in biopharmaceutical development

Ge Bai[a,*], Jared S. Bee[a], James G. Biddlecombe[b], Quanmin Chen[a], W. Thomas Leach[a]

[a] *Formulation Sciences, MedImmune LLC., One MedImmune Way, Gaithersburg, MD 20878, USA*
[b] *Formulation Sciences, MedImmune Ltd., Milstein Building, Granta Park, Cambridge CB21 6GH, UK*

ARTICLE INFO

Article history:
Received 8 September 2011
Received in revised form 8 November 2011
Accepted 28 November 2011
Available online 8 December 2011

Keywords:
Agitation stress
Shear
Protein aggregation
Computational fluid dynamics (CFD)

ABSTRACT

Agitation of small amounts of liquid is performed routinely in biopharmaceutical process, formulation, and packaging development. Protein degradation commonly results from agitation, but the specific stress responsible or degradation mechanism is usually not well understood. Characterization of the agitation stress methods is critical to identifying protein degradation mechanisms or specific sensitivities. In this study, computational fluid dynamics (CFD) was used to model agitation of 1 mL of fluid by four types of common laboratory agitation instruments, including a rotator, orbital shaker, magnetic stirrer and vortex mixer. Fluid stresses in the bulk liquid and near interfaces were identified, quantified and compared. The vortex mixer provides the most intense stresses overall, while the stir bar system presented locally intense shear proximal to the hydrophobic stir bar surface. The rotator provides gentler fluid stresses, but the air–water interfacial area and surface stresses are relatively high given its low rotational frequency. The orbital shaker provides intermediate-level stresses but with the advantage of a large stable platform for consistent vial-to-vial homogeneity. Selection of experimental agitation methods with targeted types and intensities of stresses can facilitate better understanding of protein degradation mechanisms and predictability for "real world" applications.

1. Introduction

Agitation of small liquid volumes is a common and important step in many biopharmaceutical development protocols, yet the fundamental nature of the stresses involved and the impact on protein stability are not fully understood. Agitation steps are sometimes involved in small-scale process development studies spanning upstream through fill-finish, screening methods used to optimize Drug Product formulation, container and fill-volume, and in many analytical testing methods. The purpose of agitation in these protocols varies from simple mixing of components, to increasing mass transfer (e.g. of protein to interfaces in multi-phase systems), to deliberate introduction of agitation-related stresses to accelerate protein degradation in screening experiments. Protein degradation (e.g. denaturation, aggregation or particle formation) has been widely attributed to agitation (Maa and Hsu, 1997; Mahler et al., 2005; Cromwell et al., 2006; Kiese et al., 2008; Bee et al., 2011; Kishore et al., 2011), but the specific mechanical, fluid or interfacial stress that causes degradation is rarely unequivocally identified or quantified. Many times this gap in fundamental understanding does not hinder the primary aim of the laboratory protocol, e.g. if simple mixing is desired. But when small-scale agitation studies are performed with the aim of preserving product quality, e.g. through manufacturing process or formulation design, it may be of use to identify specific stresses responsible for degradation and take into account the quantitative differences in these stresses between experimental and "real-world" conditions.

There are several commonly used vial agitation stress methods, including: shaking with a vortex mixer (Katakam et al., 1995; Katakam and Banga, 1997), orbital shaking (Kiese et al., 2008, Wang et al., 2008), magnetic stirring (Kiese et al., 2008; Lahloua et al., 2009) and end-over-end rotation (Bee et al., 2010a). During vial agitation experiments, a protein drug solution is filled into a certain type of container and attached to a vial agitation instrument to create a predefined style of motion, such as orbital motion in a horizontal plane or end-over-end rotation. The container used in this type of stressing experiment is usually the desired container of final Drug Product packaging, or a convenient container common to most formulation development laboratories such as a glass vial or centrifuge tube. One example of a formulation screening protocol to ensure robustness to shipping stresses involves shaking formulations containing various polysorbate levels in glass vials with a defined headspace on an orbital shaker (Chou et al., 2005). Similar experiments have been performed using a shipping simulator that mimics vibration frequencies and intensities common for ground transportation (Singh et al., 2006). Another protocol has been used

---

* Corresponding author. Tel.: +1 301 398 5285; fax: +1 301 398 7539.
E-mail address: Baig@medimmune.com (G. Bai).

0378-5173/$ – see front matter © 2011 Elsevier B.V. All rights reserved.
doi:10.1016/j.ijpharm.2011.11.044

Nomenclature

A_0	area of interface in a mesh cell (m^2)
A_{A-L}	area of air–liquid interface (m^2)
A_{S-L}	area of solid–liquid interface (m^2)
f	subscript for wetted mesh cell surface (dimensionless)
F	fraction of mesh cell volume occupied by fluid (dimensionless)
G	air–liquid interface regeneration rate ($mL\,s^{-1}$)
G_c	air–liquid interface generation rate in one mesh cell (s^{-1})
L	characteristic length (m)
n	liquid recirculation intensity (dimensionless)
N	agitation frequency (rotations/s)
P	pressure (N/m^2)
$\bar{P}$	local average pressure (N/m^2)
R_e	Reynolds number ($=\rho NL^2/\mu$) (dimensionless)
S_{ij}	component of the rate-of-deformation tensor (s^{-1})
S	rate-of-deformation tensor (s^{-1})
t	time (s)
T	total shear (dimensionless)
U	velocity vector ($m\,s^{-1}$)
U_i	velocity in the i direction ($m\,s^{-1}$)
$\overline{U_i}$	time-average velocity magnitude in the i direction ($m\,s^{-1}$)
U_n	velocity component normal to the interface ($m\,s^{-1}$)
V	total fluid volume (m^3)
V_c	volume of a mesh cell (m^3)
x_i, x_j	coordinates in the i and j directions
Greek symbols	
$\dot{\gamma}$	magnitude of shear rate (s^{-1})
$\dot{\gamma}_{A-L}$	magnitude of volume averaged shear rate near air–liquid interface (s^{-1})
$\dot{\gamma}_{A-L}^{max}$	maximum shear rate near air–liquid interface (s^{-1})
$\dot{\gamma}_{S-L}$	magnitude of volume averaged shear rate near solid–liquid interface (s^{-1})
$\dot{\gamma}_{S-L}^{max}$	maximum shear rate near solid–liquid interface (s^{-1})
$\dot{\gamma}_{sys}$	magnitude of system volume averaged shear rate s (s^{-1})
$\dot{\gamma}_{sys}^{max}$	system maximum shear rate (s^{-1})
μ	liquid viscosity ($kg\,m^{-1}\,s^{-1}$)
ρ	liquid density ($kg\,m^{-3}$)
τ	stress tensor ($kg\,m^{-1}\,s^{-2}$)

to optimize formulations to minimize protein aggregation in the presence of silicone oil, which is a common component on syringe and stopper surfaces. In this example, a silicone oil emulsion was spiked into a glass vial containing a small volume of formulated protein and shaken on an orbital shaker (Thirumangalathu et al., 2009). The fill volume of a glass vial has been similarly optimized to minimize protein aggregation and particle formation by shaking studies using a horizontal to-and-from motion (Eppler et al., 2010). To date, there are no compendial methods for any of these stress studies. In part, this is likely due to the complexities of clearly predicting which components of agitation stress are most detrimental to the stability of protein solutions and which would be the most relevant scale-down model for each type of real-world agitation stress.

The most commonly reported protein degradation products that arise in agitation studies are aggregates, and subvisible and visible particles. These degradants are also commonly seen upon protein exposure to many other mechanical and physical stresses such as stirring, pumping, concentration, tangential flow filtration (TFF), freeze–thaw and lyophilization (Wang, 1999; Cromwell et al., 2006; Rosenberg et al., 2009). There are many reports where commercial proteins have been impacted by agitation stress in particular. In two studies with monoclonal antibodies (mAbs), stirring was found to generate more aggregates than shaking (Mahler et al., 2005; Kiese et al., 2008). In another case the particles, in part, were found to contain intermolecular disulfide bonds formed from the buried cysteines of an antibody after it was exposed to agitation stress (Brych et al., 2010). Growth of insulin fibril particles in bulk solution was proposed to be preceded by generation of partially unfolded monomers caused by stress at the air–water interface during agitation (Nielsen et al., 2001). In another case, low shear bubbling and foaming resulted in aggregation of human growth hormone (Maa and Hsu, 1997). In many cases, addition of polysorbate surfactants can minimize or eliminate particle formation of proteins exposed to agitation or shear. This has been suggested to be due to the ability of surfactants to protect the protein from adsorbing and unfolding at the air–water interface (Patapoff and Esue, 2009).

The potential effects of these aggregates on product quality are numerous. Bioactivity of protein could be potentially reduced or lost due to aggregation (Becker et al., 1987; Branden and Tooze, 1998) Aggregates may also potentially result in immune reactions in patients (Rougeot et al., 1991; Patten and Schellekens, 2003; Schellekens, 2005; Rosenberg, 2006). Agitation stress can also lead to an unacceptable change in appearance of the protein drug due to opalescence or particles even though they may constitute a very small mass percentage of the actual product. Thus, understanding and control of agitation stress is an integral part of bringing high quality biopharmaceuticals to patients.

There are several different aspects of agitation mechanical stress that are potential causative factors of aggregation and particle formation of therapeutic proteins. The factors may include: increases in reactive collisions due to enhanced mass transport and mixing (Treuheit et al., 2002; Harrison et al., 2003), shear rate and total shear (Maa and Hsu, 1996), air–liquid interface and synergetic effect of shear rate and air–liquid interface (Maa and Hsu, 1997; Colombié et al., 2001; Chou et al., 2005; Mahler et al., 2005; Bee et al., 2009a; Thomas and Geer, 2011), solid–liquid interface and synergetic effect of shear rate and solid–liquid interface (Tzannis et al., 1997; Colombié et al., 2001; Biddlecombe et al., 2007, 2009; Bee et al., 2009b; Thomas and Geer, 2011), air–liquid interface regeneration (Bee et al., 2010a) and cavitation (Gulseren et al., 2007; Van Reis and Zydney, 2007). Because these different factors are difficult to directly and individually isolate, measure and compare in experimental systems, it is frequently not clear which of these are most detrimental to protein stability. It is also not clear what the fundamental differences are in specific stress intensities generated among the different types of laboratory agitation instruments, and what the impact of agitation frequency is for each method. Clearly these uncertainties hinder the ability to make inferences from laboratory experiments to stability under "real world" conditions. This is where computational fluid dynamics (CFD) can contribute by providing fundamental insights not easily determined experimentally.

Computational fluid dynamics (CFD) is a numerical method that studies fluid behavior by solving conservation equations of momentum, mass and energy. It provides an alternative for researchers to solve fluid related challenges when no experimental method to measure the appropriate parameters (e.g. shear rate stress in different points of a vial being vortexed) can be practically applied. CFD has already been successfully applied in different areas in the pharmaceutical and biopharmaceutical industries to study hydrodynamic problems recently including dissolution testing (Bai et al., 2007a, 2007b, 2011; Bai and Armenante, 2009), lyophilization (Alexeenko et al., 2009), mixing (Akiti et al., 2005; Bai and Armenante, 2008), and pumping (Song et al., 2003) with substantial insightful benefits. It provides insight and information which cannot easily or simply be obtained from experimental methods. CFD is unique in its ability to discern specific agitation mechanical stresses and to calculate the intensity of each stress brought to a protein by different vial agitation methods. Therefore, the purpose of this study is to apply CFD to model the hydrodynamics of liquid in a glass container agitated with different vial agitation instruments at different agitation frequencies to (a) identify the different types of mechanical and interfacial stresses, (b) quantify these stresses, (c) identify the impact from agitation frequency on identified stresses, and (d) identify similarities and/or differences among commonly used vial agitation methods.

2. Materials and methods

2.1. Container, closure and fluid

The geometry of the glass container modeled in this work is based on a Schott 3 mL glass vial (Part No.: 38000316) with a nominal inner diameter of 14.55 mm. The geometry of the stopper modeled in this work is based on West Teflon Faced stopper (Part No.: 10124660). The volume of liquid in the glass vial is fixed to 1 mL in this work. The fluid properties of protein drugs in solution such as density, viscosity, surface tension may vary widely due to the variability in protein molecular structure, protein concentration and excipients used in different liquid formulations. The fluid properties used in this work are based on those of water at 25 °C.

2.2. Lab vial agitation instruments

The four lab agitation instruments modeled in this work are listed below:

- orbital shaker (Techne USA, TSSL1);
- magnetic stirrer (VWR Multi-Position Magnetic Stirrers, Cat No.: 12621-046) with magnetic stir bar (VWR® Spinbar® Micro Stir Bar, Cat No.: 58948-353);
- vortex mixer (VWR Signature Digital Vortex Mixer, Cat. No.: 14005-824);
- rotator (Scientific Industries ROTO Shake Genie).

Both the orbital shaker and vortex mixer provide the same type of motion to a vial: orbital motion in a horizontal plane. The differences are orbital diameter and agitation frequency range. The orbital shaker has an orbital diameter of 16 mm and an agitation frequency range of 30–300 rpm. The vortex mixer has an orbital diameter of 4.9 mm and an agitation frequency range of 500–3200 rpm. The magnetic stir bar has a length of 8 mm. Its cross section is a square shape with an edge length of 1.5 mm. The main flow generated by the magnetic stir bar in the glass vial is also in the horizontal plane. The agitation frequency range of stirring is 60–1400 rpm, which is controlled digitally by the magnetic stirrer. There are a lot of ways to place a glass vial on a rotator. In this work, only end-over-end rotation of the vial was modeled by CFD. The glass vial is oriented perpendicular to the rotator centerline axis to achieve a tumbling motion. The vial center follows a circular path and the edge of the vial is 25.4 mm away from the rotator centerline. When the glass vial is upright vertically, the horizontal position of the axis is at the same level of the mid point between the top edge of the stopper and the bottom edge of the glass vial. The agitation frequency of the rotator ranges from 5 to 35 rpm. Table 1 lists the agitation frequencies of each lab agitation instrument modeled in this work. Although the vortex mixer and magnetic stirrer can operate above 1000 rpm, vigorous agitations with frequencies higher than 1000 rpm are rarely used in stress studies. Thus, in this work, the maximum agitation frequency modeled is 1000 rpm for the vortex mixer and magnetic stirrer.

Table 1
Agitation methods, agitation frequency ranges and CFD modeled agitation frequencies.

Vial agitation methods	Agitation frequency range (rpm)	Agitation frequency modeled in this work (rpm)
Rotator	5–35	10, 20, 35
Orbital shaker	60–300	100, 200, 300
Magnetic stirrer	60–1400	100, 200, 300, 600, 1000
Vortex mixer	500–3200	600, 800,1000

2.3. Computational methodology

Flow-3D® (Flow Science Inc., Santa Fe, NM), a commercial CFD package, was used to analyze the hydrodynamics of the fluid. Like other commercially available CFD packages, Flow-3D® is developed based on a finite volume method. Conservation equations of momentum, mass and energy are solved at thousands, sometimes even million locations within the fluid domain. These locations are generated by dividing the fluid domain into finite volumes in a process referred to as meshing of the fluid domain. The conservation equations are solved in each mesh cell using discretization techniques (Pantankar, 1983; Anderson et al., 1984). In Cartesian coordinates, the time-averaged continuity equation for an incompressible fluid is written using the summation convention and can be written as:

$$\frac{\partial \overline{U_i}}{\partial x_i} = 0 \tag{1}$$

The time-averaged momentum equation, which can be used for the prediction of the velocities in turbulent flow, is:

$$\frac{\partial \bar{U}_i}{\partial t} + \overline{U_j}\frac{\partial \overline{U_i}}{\partial x_j} = -\frac{1}{\rho}\frac{\partial \bar{P}}{\partial x_i} + \nu\nabla^2\overline{U_i} + g_i - \frac{\partial}{\partial x_j}\left(\overline{U_i'U_j'}\right) \tag{2}$$

The last term in this equation represents the Reynolds stresses, containing the product of the fluctuating velocity components. For laminar flow it equals to zero.

After the whole fluid domain is resolved, various fluid dynamics information including velocities, pressure, temperature, density, energy are available for analysis. Although there are differences among commercially available CFD packages in terms of accuracy, available turbulence models, and user interface, most of them follow the same principles mentioned above to conduct fluid dynamics modeling. The standard Flow-3D® solver was customized to serve the purpose of this work. The version of the Flow-3D® solver used for this work is 9.4.s.

Flow-3D® adapts the “free gridding” method to generate mesh cells. In Flow-3D®, geometry and mesh cells are independent and can be freely changed. Only rectangular mesh cells are used by Flow-3D® instead of body-fitted mesh cells with different shapes, which provide simplicity of meshing (Barkhudarov, 2004; Wei, 2005). Flow-3D® also incorporates Fractional Area Volume Obstacle Representation method (FAVOR™). With this method, fractional areas and fractional volumes are computed to define obstacles placed within a rectangular mesh cell without sacrificing numerical accuracy (Sicilian, 1990; Wei, 2005). Solid boundaries can be identified automatically after the geometries of solid are imported and meshed. Fig. 1 shows the schematics of rectangular shaped mesh cells with side and top views for rotator simulations. The red dashed circle represents the rotation path of a vial on a rotator. When simulating motion, fluids and solid objects both move throughout the stationary mesh. The actual simulations use

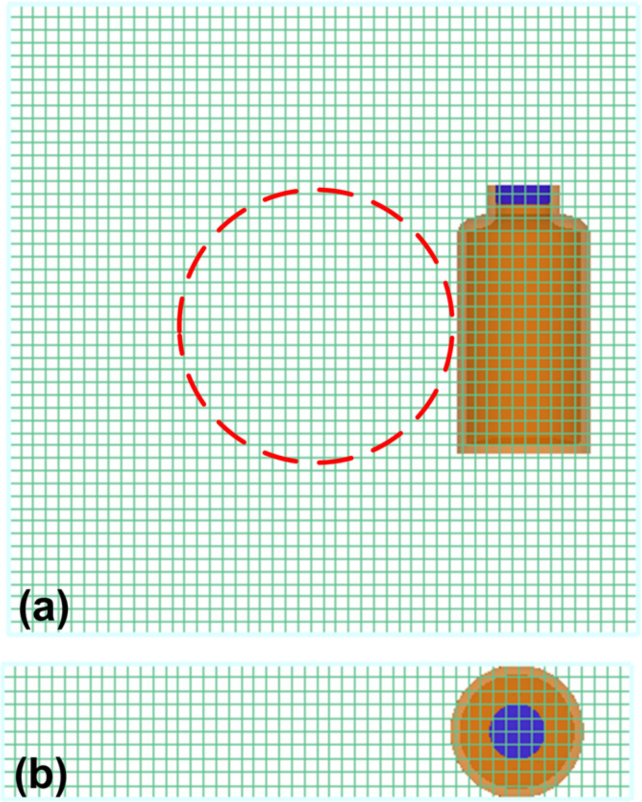

Fig. 1. Schematics of Flow-3D® mesh cells for the rotator: (a) side view and (b) top view. (For interpretation of the references to color in the text, the reader is referred to the web version of this article.)

much denser mesh cells. Flow-3D® applies Volume of Fluid (VOF) technique to model free surfaces. It implements all three VOF ingredients: a scheme to locate the surface, an algorithm to track the surface as a sharp interface moving through a computational grid, and a means of applying boundary conditions at the surface (Hirt and Nichols, 1981). These features mentioned above enable Flow-3D® to suitably model fluid systems associated with moving solid boundaries and free surfaces and therefore fit the needs of this work.

However, there are numerical limitations of Flow-3D® when simulating solid boundaries passing through fixed mesh grid for high frequency orbital motions such as with the vortex mixer. In this case, the grid can be anchored to the moving solid object (the vial in this case) such that the grid moves in an orbital motion. The moving grid is referred to as the non-inertial reference frame. In this work, simulations for the vortex mixer were performed with the non-inertial reference frame approach. For consistency, the orbital shaker is also simulated with non-inertial reference frame approach. With this approach, numerical errors due to solid boundaries passing rapidly through a fixed mesh are avoided.

2.4. Area of interfaces

For the calculation of the area of solid–liquid interfaces inside a rectangular mesh cell, the Gauss theorem (Byron and Fuller, 1992) is applied by Flow-3D®:

$$\int_{V_c} \nabla \cdot U \, dv = \oint_S nU \, ds \tag{3}$$

where V_c is the volume of the rectangular mesh cell, S is the surface of the rectangular mesh cell, U is velocity vector, and n is the outer normal to the surface S. In Flow-3D®, the mesh cell is partially blocked, with only a part of its volume and faces open to the flow. The fractional open areas on all six sides of the mesh cell are known: A_1 (lower x), A_2 (upper x), A_3 (lower y), . . ., A_6 (upper z). The above integration is done only over open portions of both volume and area, so the surface S includes open faces and the internal solid surface, the area of which is A_0. Eq. (3) can be solved to obtain the value of A_0. The summation of A_0 across all mesh cells that contain the solid–liquid interface generates the total area of solid–liquid interface. Flow-3D® applies a similar approach to calculate the area of air–liquid interface. The roughness of solid surfaces may have a significant impact on the area of solid–liquid interface and protein aggregation (Biddlecombe et al., 2009). However, in this work, the solid surface is modeled as perfectly smooth since capturing roughness and its impact on agitation stresses is beyond the capability of Flow-3D®.

2.5. System volume averaged shear rate

Bulk fluid strain rate (expressed in units of reciprocal seconds) represents the rate at which the velocity varies with distance when moving away from the point of interest. In most of protein stability and formulation literature, it is also termed “shear rate”. To facilitate accessibility to the target readers of this work, the term “shear rate” is used throughout this work.

The shear stress tensor, τ, is related to the rate-of-deformation tensor, S, through the equation:

$$\tau = -\mu S \tag{4}$$

where μ is the fluid viscosity. For an incompressible Newtonian fluid, the components of the rate-of-deformation tensor, S_{ij}, are given by (Bird et al., 2002):

$$S_{ij} = \frac{\partial U_i}{\partial x_j} + \frac{\partial U_j}{\partial x_i} \tag{5}$$

Then, the local value of magnitude of the shear rate (or “shear rate”), $\dot{\gamma}$, is defined as:

$$\dot{\gamma} = |S| = \sqrt{\frac{1}{2}\sum_i \sum_j S_{ij}^2} \tag{6}$$

The system volume averaged shear rate for a given fluid system, $\dot{\gamma}_{sys}$, is calculated by the equation:

$$\dot{\gamma}_{sys} = \frac{1}{V}\int_V \dot{\gamma} \, dv = \frac{1}{V}\sum (F \cdot \dot{\gamma} \cdot V_c)_{i,j,k} \tag{7}$$

where V is the fluid volume in the whole fluid domain, dv is the volume element of fluid, and F is the fraction of fluid in a mesh cell. The summation is carried out over all mesh cells in the computational fluid domain at every time step.

2.6. Volume averaged shear rate near the air–liquid and solid–liquid interfaces

Volume averaged shear rate near the air–liquid interface, $\dot{\gamma}_{A-L}$, and solid–liquid interface, $\dot{\gamma}_{S-L}$, are calculated with similar approaches as the system volume averaged shear rate, $\dot{\gamma}_{sys}$. The only differences are that the integration of shear rates are only performed in the mesh cells that contain the interfaces and the averaging is performed against the total liquid volume of mesh cells that contain the interfaces. $\dot{\gamma}_{A-L}$ and $\dot{\gamma}_{S-L}$ are the shear rate of the layer of liquid which is very close to the interfaces. The degree of closeness depends on the size of the mesh cell and the exact location of the interface in the mesh cell. The thickness of this liquid layer near the interfaces is no larger than 170 μm, which is the largest size of mesh cell used in this work.

2.7. System maximum shear rate and maximum shear rate near interfaces

Flow-3D® calculates shear rate values for each mesh cell in the fluid domain. It also sorts the shear rate values to identify the maximum shear rate for the whole fluid domain, and for the mesh cells that contain air–liquid and solid–liquid interfaces at each time step. Thus the system maximum shear rate, $\dot{\gamma}_{sys}^{\max}$, the maximum shear rate near air–liquid interface, $\dot{\gamma}_{A-L}^{\max}$, and the maximum shear rate near solid–liquid interface, $\dot{\gamma}_{S-L}^{\max}$, can be obtained and compared.

2.8. Total shear

Total shear, T, representing the cumulative time effect of shear rate, is calculated based on the following equation:

$$T = \dot{\gamma}_{sys} t \tag{8}$$

where t is the total agitation time in seconds. In this work, the system volume averaged shear rate, $\dot{\gamma}_{sys}$, is used to calculate the total shear of the whole fluid domain.

2.9. Air–liquid interface regeneration rate

The air–liquid interface generation rate in a mesh cell containing an air–liquid interface is defined as:

$$G_c = \frac{U_n A_0}{V_c} + (\nabla \cdot \vec{U})_f \tag{9}$$

where U_n is the fluid velocity component normal to the interface, A_0 is the interface area in the mesh cell, V_c is the volume of the mesh cell, and subscript f represents wetted cell surfaces. The first term on the right-hand side of this equation describes the inflow of fluid into the mesh cell in the direction normal to the air–liquid interface. The second (divergence) term in the expression is computed only over the wetted faces of the mesh cell and thus represents the change of fluid volume in the mesh cell. The sum of the two terms represents the amount of fluid (per unit volume and time) that arrives at a surface mesh cell and spreads along the air–liquid interface. This generation term therefore captures the mass addition to newly created areas of the air–liquid interface due to surface expansions and turnover. It includes addition not only at the surface but also in the layer of liquid within the mesh cells at the surface, thus convection very near the interface is also captured. The generation rate term is only tabulated for cells where it is positive (material arriving at the interface) and is not tabulated when it is negative (material depletion at the interface). It is assumed that the positive and negative terms will cancel each other at steady state since the air–liquid surface is not growing overall, i.e. an equal quantity of material is added and depleted for no net surface area change. The integration of G_c over all mesh cells containing air–liquid interface therefore generates the air–liquid interface regeneration rate, G, with a unit of $\mathrm{mL\,s^{-1}}$. It represents the volume of fluid reaching the layer of mesh cells containing air–liquid interface per unit time.

$$G = \sum_{i=1}^{n} G_{ci} F_i V_{ci} \tag{10}$$

2.10. Liquid recirculation intensity

Through air–liquid interface regeneration, drug substance can be brought to/near the air–liquid interface (the layer of mesh cells that contain air–liquid interface) from the bulk liquid during vial agitation. The intensity of recirculation of liquid from bulk to/near air–liquid interface can be calculated with the following equation:

$$n = \frac{Gt}{V} \tag{11}$$

where t is the total agitation time and V is the total volume of liquid.

2.11. Cavitation potential

When cavitation occurs, the local pressure of fluid drops below its vapor pressure, resulting in flashing of the liquid. Cavitation can create high temperature and shock waves which can possibly generate damage to protein molecule and lead to aggregation and/or particle formation (Gulseren et al., 2007; Van Reis and Zydney, 2007). Cavitation potential is monitored throughout whole fluid domain at each time step by comparing the local pressure with the vapor pressure of water at 25 °C, which is 23.76 mmHg. Only when the local fluid pressure drops below the vapor pressure, there is a possibility that cavitation would occur. The difference between the vapor pressure and local pressure of fluid is defined as cavitation potential. Anytime this value is greater than zero, cavitation could potentially occur.

3. Results and discussion

3.1. CFD model optimization

3.1.1. Determination of the simulation flow model

The Reynolds number, R_e, was calculated for each of the lab agitation instruments at the highest agitation frequency covered in this study to determine if a turbulence model is needed. The equation used to calculate the Reynolds number is:

$$R_e = \frac{L^2 N \rho}{\mu} \tag{12}$$

where L is the characteristic length of the fluid system, n is the agitation frequency of the fluid system, and ρ is the density of the fluid (Tchobanoglous et al., 2003). The characteristic length is selected as the inner diameter of the glass vial in all cases except for the magnetic stirrer. In this case, the diameter of the magnetic stir bar is selected instead. The Reynolds number of each agitation method at the highest agitation frequency in this work is listed in Table 2(a). Only the Reynolds number of vortex mixer at 1000 rpm lies in the transitional flow zone (2300–4000). All other modeled fluid systems have Reynolds numbers that lie in the laminar flow zone (<2300). Flow-3D® provides turbulence models that are designed for modeling fully turbulent flow. Fluid agitated with the vortex mixer at 1000 rpm was modeled as laminar flow in this work for consistency of comparison.

3.1.2. Validation of the CFD model

Ideally, CFD simulation results (e.g. velocity profiles) should be compared against experimental results for modeling validation purposes. However, due to the very small size of the fluid domain modeled in this work and the fact that the fluid motion frequencies are high, conventional experimental techniques such as Laser Doppler Velocimetry (Bai et al., 2007a, 2007b, 2011) cannot be applied to measure the velocity profiles. Instead, in this work, the shapes of air–liquid interfaces were compared between experiments and simulations. In Fig. 2(a), the shape of the air–liquid interface for fluid agitated with the orbital shaker at 300 rpm is compared between CFD simulation and experiment. In Fig. 2(b), the shape of the air–liquid interface for fluid agitated with the rotator at 35 rpm (55° angle from the vertical position) is compared between CFD simulation and experiment. CFD simulations capture the shape of the air–liquid interfaces well in these two cases. This provides

Table 2
Comparison of agitation stresses at the highest agitation frequencies.

Agitation methods and agitation frequencies	(a) System				(b) Air–liquid interface					(c) Solid–liquid interface		
	R_e	$\dot{\gamma}_{sys}$ (s^{-1})	$\dot{\gamma}_{sys}^{max}$ (s^{-1})	T for 24 h	$\dot{\gamma}_{A-L}$ (s^{-1})	$\dot{\gamma}_{A-L}^{max}$ (s^{-1})	Normalized A_{A-L}	G (mL s^{-1})	n for 24 h	$\dot{\gamma}_{S-L}$ (s^{-1})	$\dot{\gamma}_{S-L}^{max}$ (s^{-1})	Normalized A_{S-L}
Rotator (35 rpm)	229.0	30.45	1711	2.600×10^6	23.18	1433	1.630	0.1400	1.242×10^4	32.68	1033	1.060
Orbital shaker (300 rpm)	1058	83.35	2016	7.200×10^6	90.40	1776	2.290	0.2500	2.160×10^4	143.2	1173	1.310
Magnetic stirrer (1000 rpm)	1067	115.7	3040	1.000×10^7	70.88	1360	1.300	0.2600	2.247×10^4	99.45 (407.7[a])	1596 (3040[a])	1.090 (1.000[a])
Vortex mixer (1000 rpm)	3529	384.8	8315	3.300×10^8	209.9	6905	7.090	2.340	2.022×10^5	432.4	3126	2.580

[a] For solid–liquid interface at the magnetic stir bar surface.

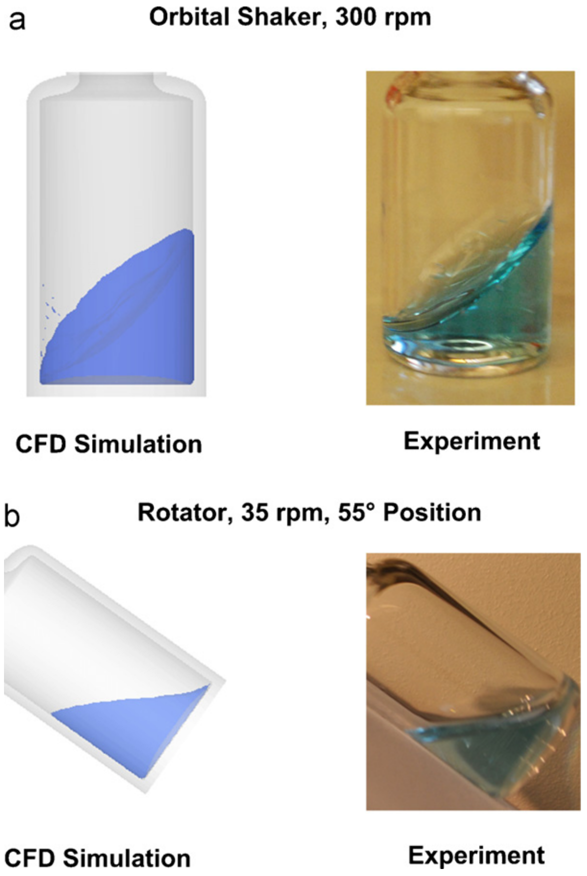

Fig. 2. Comparison of the shape of fluid free surface between CFD simulation and experiment for (a) orbital shaker at 300 rpm at steady state and (b) rotator at 35 rpm, 55° position.

assurance that the CFD model used in this work can predict the fluid behaviors accurately. For the magnetic stirrer, the shape of air–liquid interface is not significantly altered relative to static conditions at low agitation frequencies. At high agitation frequencies, for both the magnetic stirrer and vortex mixer, it is very difficult to clearly capture the exact position of the magnetic stir bar and shape of the air–liquid interface with a camera to compare with CFD simulation. However, visual observations indicate that CFD simulation predict the general shape of the air–liquid interfaces well in each of these two cases.

3.1.3. Data processing for comparison

The orbital shaker, magnetic stirrer and vortex mixer mainly generate tangential circular motions and fluid flow in the horizontal plane. Each of these systems reaches steady state within 4 s following startup. In this work, the criterion for defining steady state is when the fluctuation of the system mean kinetic energy is less than 1%. When steady state is reached, all parameters studied in this work such as system volume averaged shear rate remain nearly constant as shown in Fig. 3(a). The shape of the agitated liquid also does not change appreciably after steady state is reached. In agitation stress studies, vials are commonly agitated on these instruments for several hours, thus the less than 4 s startup period is likely insignificant when studying the overall stress to a protein. Among these various horizontal vial agitation methods at various agitation frequencies, the differences are the time it takes to reach steady state and the intensities of the studied parameters after steady state is reached. For the systems that reach steady state (i.e. the orbital shaker, magnetic stirrer and vortex mixer), the values

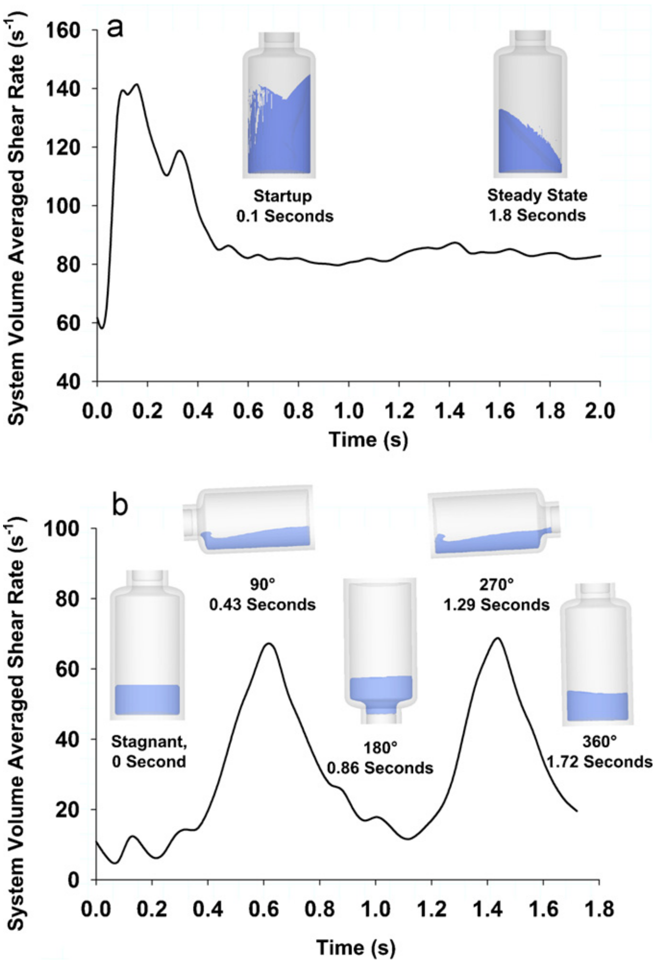

Fig. 3. Comparison between systems that can and cannot reach steady state during agitation on fluid free surface shape and system volume averaged shear rate: (a) orbital shaker at 300 rpm and (b) rotator at 35 rpm.

of studied parameters were averaged over a one second period of time after steady state is reached for the purpose of comparison.

In contrast to the above systems, the rotator rotates vials end-over-end and mainly generates cyclical motions of fluid within an asymmetric cross section of the vial. In this case, the fluid flows from one end of the vial to the other as the vial rotates and never reaches steady state. The studied parameters in this work change over time by following sinusoidal curves as shown in Fig. 3(b). The changing shape of fluid in a rotated vial at 35 rpm is also shown in the same figure. In order to make comparisons across different agitation methods, the raw data from the rotator simulations were further processed. The values of studied parameters in this work were integrated using the trapezoid rule and averaged over the period of time for one complete rotation. For the maximum shear rates (within the system and near interfaces), the highest values over a full rotation were picked for comparison with agitation methods that can reach steady state, no averaging was performed.

3.2. Flow patterns

Fig. 4 depicts a cross section of a vial on the rotator at 45°, 90°, 135° and 180° positions. The vial rotates counter clockwise at 35 rpm. The figure panels show a 2D fluid velocity vector map colored by velocity magnitude where the in-plane velocity vector components are represented. Combined with the fluid free surface shape shown in Fig. 3(b), the flow pattern of rotator is clear. The rotator operates at a relatively slow frequency such that the centrifugal force is not significant. The fluid motion is analogous the water being poured out of one end of the vial and subsequently impinging on the other end. The velocity of the impinging fluid depends on the rotation frequency and rotation diameter. When the vial rotates from 0° to 90° (upright vertical position to horizontal position), relatively to the vial, the fluid flows uphill, and the fluid reside on the side of the vial at the 90° position. Since the vial is still rotating after it reaches 90° position, the fluid continues flow towards the stopper side of the vial. When the vial rotates from 90° to 180° (horizontal position to inverted vertical position), gravity accelerates the fluid in addition to the rotational forces, which results in relatively higher velocity magnitude of fluid velocity and relatively more complicated flow directions as shown by the 135° position vector plots in Fig. 4. The fluid flows downhill along the vial wall and impinges on to the stopper. Eddies may exist but the flow is believed to be laminar in general. When the vial rotates from 180° to 360°, the fluid behaves similarly as it does from 0° to 180° but the directions of the flow are the opposite. As shown in Fig. 3(b), the system volume averaged shear rate, $\dot{\gamma}_{sys}$, reaches its peak values when the vial is at 90° and 270° (horizontal) positions as in these positions, the fluid experience highest change in terms of velocity magnitudes.

Fig. 5 shows the 3D fluid shape and 2D velocity vector maps for the magnetic stirrer at 1000 rpm at steady state. It shows that even at its highest agitation frequency, 1000 rpm, the fluid does not have sufficient centrifugal momentum to "climb" the walls significantly. The fluid is dispersed nearly uniformly around the entire vial circumference, which is in contrast to the lop-sided fluid bodies observed with the orbital shaker and vortex mixer. Similar to the mixing system with a two-blade impeller (Bai et al., 2007a), the primary flow in a magnetic stirred vial is tangential flow in the horizontal plane as shown by the velocity vectors at $Z = 0.5$ cm. The flow patterns in any other horizontal planes at any other Z locations are similar. The secondary flows are in the vertical planes which have lower velocities than in horizontal plane, indicating much weaker flow. In these vertical planes, the fluid next to the tips of the magnetic stir bar is pushed towards to the vial wall. After the fluid hits the vial wall, the fluid splits. One portion flows upwards and one portion flows downwards. The upwards flowing fluid "climbs" up against the vial wall, although not much, and then flows back towards the vial center. The downward flowing fluid hits the vial bottom almost immediately and flows back towards the vial center. Thus, two recirculation loops (one along air–liquid interface, the other along vial bottom) form on both sides of the magnetic stir bar in the vertical planes. The convective mixing of the fluid in magnetic stirrer vial is mainly due to the secondary flow in vertical planes.

Fig. 6 shows the 3D fluid shape and 2D velocity vector maps colored by velocity magnitude for the orbital shaker at 300 rpm at steady state. Fig. 7 shows the similar plots for vortex mixer at 1000 rpm at steady state. The orbital shaker and vortex mixer impart similar types of motion to the vial; the differences are agitation frequencies and orbital diameters. In both cases, the vial passes through a circular orbit but does not spin. For the orbital shaker, as the vial orbits, a centrifugal force is generated that causes the fluid to disperse against the vial wall. Thus the fluid "climbs" towards the upper portions of the vial wall unevenly and the air–liquid interface is elongated vertically. At 300 rpm, the fluid can climb up to about the half height of the vial along one side of the vial wall as shown by the 3D and $Y = 0$ plane in Fig. 6. A horizontal cross section of the fluid at $Z = 1.0$ cm above the vial bottom shows a "crescent" shape of fluid. Here, a fluid layer slides around the inner circumference of the vial. Because the vial does not spin, the fluid nearest the wall is "held back" while the bulk passes over it, creating a "conveyor belt" type of convective current. The same type of "conveyor belt" current is found in the vortex mixer in Fig. 7, but the fluid layer is, on average,

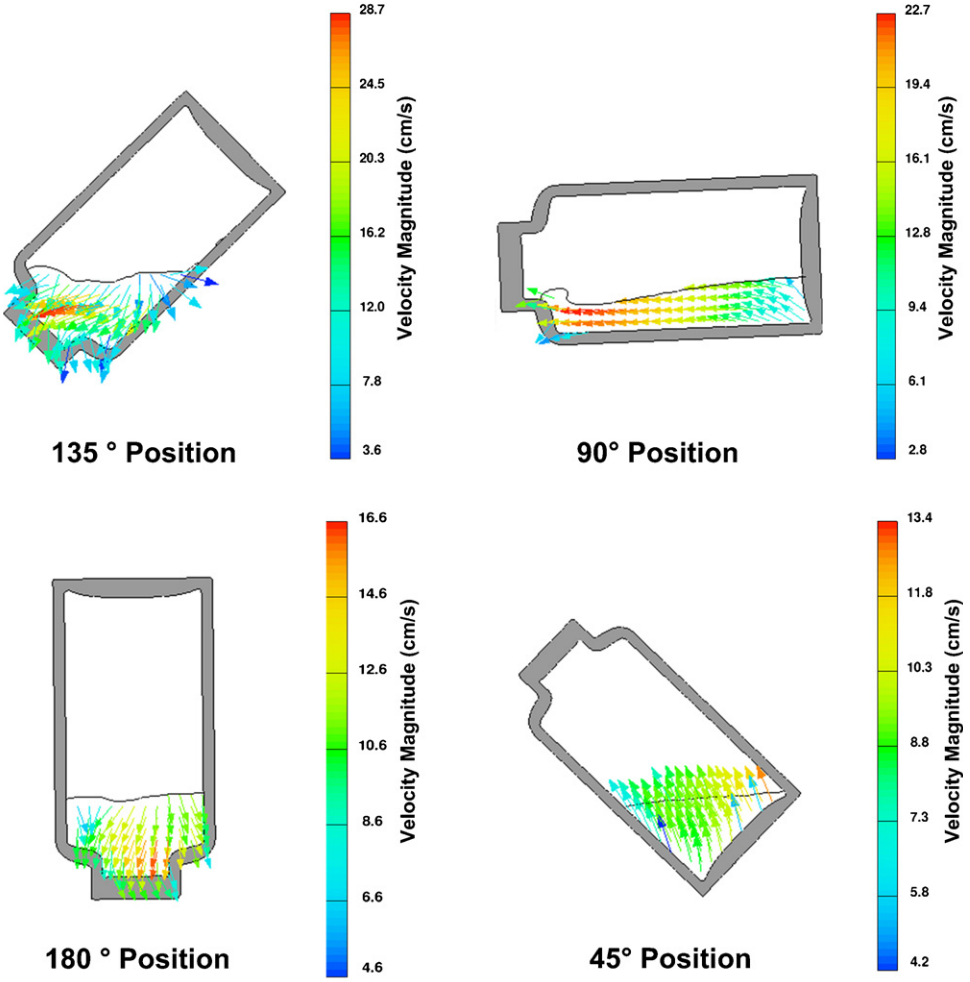

Fig. 4. Flow patterns of the rotator at 35 rpm: 45°, 90°, 135° and 180° positions.

much thinner and spread over a greater span of the vial wall. The flow patterns in the vertical planes are relatively weaker for both the orbital shaker and the vortex mixer. Overall, the flow patterns are much more irregular and non-uniform in direction for the vortex mixer. Thus no discernible secondary current can be assigned to the vortex mixer, only a high level of mixing between horizontal layers and from the bulk to the interfaces can be expected.

3.3. *Shear rates*

3.3.1. *Visualization of instantaneous shear near interfaces*

Fig. 8 shows the instantaneous shear rate for each system near interfaces at their highest agitation frequencies. The fluid body is non-transparent in these images, thus the shear rates are visualized from the mesh cells at the surfaces. The highest shear rate value on the color bar is 300 s^{-1}. Red color represents shear rate magnitude 300 s^{-1} and above, and some of the values are considerably above 300 s^{-1}, as seen in Table 2. For the orbital shaker, high shear rate values are located at the air–liquid interface near the vial wall and in a small area in the center of the air–liquid surface. For the magnetic stirrer, higher shear rate values are located near vial wall at about the same level of the magnetic stir bar, but over a smaller area compared to orbital shaker. At the air–liquid interface, a small area of red color can be observed in the center where the near-surface fluid is dispersed into the bulk by the stir bar. For the vortex mixer, the fluid “climbs” up very high along the vial wall, reaching the inside of the vial “shoulder”. Much larger area of high shear can be observed near the vial wall compared to all other three agitation systems. Similarly, much larger red area can be observed at its air–liquid interface from the top view. This indicates that the vortexed fluid system experiences much larger shear rates at the interfaces than the other agitation methods. The rotator has the lowest shear rate near interfaces among all agitation systems mainly due to its very low agitation frequency. The highest shear rate (green to yellow color) is near the stopper where the fluid has highest velocities as shown in Fig. 4.

3.3.2. *System volume averaged shear rate*

Fig. 9 shows a comparison of the system volume averaged shear rate, $\dot{\gamma}_{sys}$, of the whole fluid domain among agitation methods at different agitation frequencies. For all agitation methods, $\dot{\gamma}_{sys}$ increases approximately linearly with agitation frequency except for the orbital shaker. At the maximum agitation frequencies simulated, the rank ordering of equipment with respect to $\dot{\gamma}_{sys}$ is: vortex mixer ≫ magnetic stirrer > orbital shaker > rotator (Table 2(a)). The volume averaged shear rate generated by the rotator has the steepest increase with agitation frequency increase, but this instrument is limited to low agitation frequencies. For the orbital shaker, the volume averaged shear rate climbed gently with increasing agitation frequency from 100 rpm to 200 rpm but at a much steeper rate from 200 rpm to 300 rpm. This inflection in the trend coincides with the centrifugal dispersion of the fluid vertically along the vial wall. It may indicate that the effectiveness of agitation for the non-symmetric fluid body in a rotational orbit is greater than

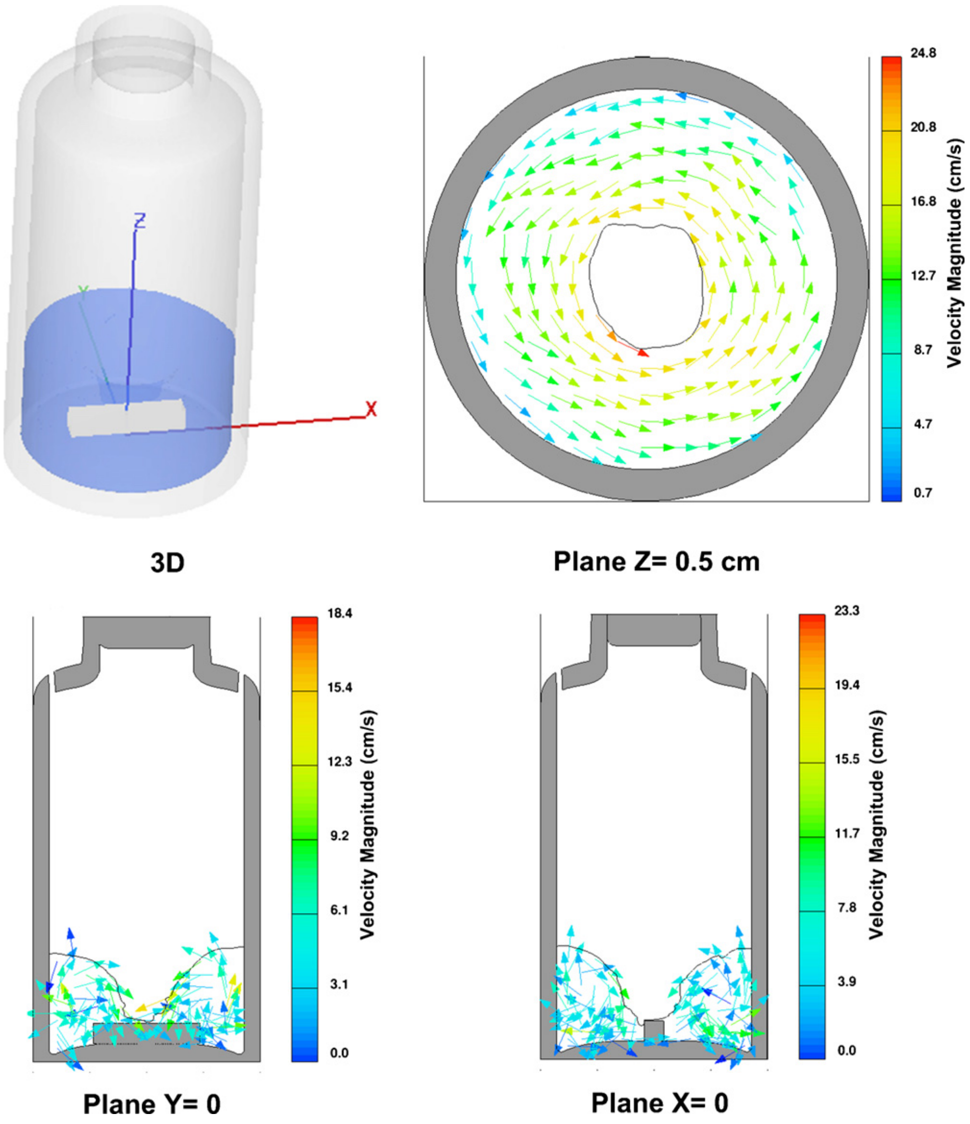

Fig. 5. Flow patterns of the magnetic stirrer at 1000 rpm at steady state (cm s^{-1}).

for the cylindrical plug shaped fluid body at lower agitation frequencies. The capability of generating $\dot{\gamma}_{sys}$ for the vortex mixer is similar to that of the orbital shaker 300 rpm and beyond, i.e. they lie on the same approximate curve, although the vortex operates at a much higher agitation frequency range. The magnetic stirrer generates much lower volume averaged shear rate at the same agitation frequency compared to orbital shaker and vortex mixer when agitation frequency is above 300 rpm. It is about 2.2 times lower at 300 rpm compared to orbital shaker (26.07 s^{-1} vs. 83.35 s^{-1}) and about 2.3 times lower at 1000 rpm compared to vortex mixer (115.69 s^{-1} vs. 384.77 s^{-1}). The vortex mixer provides the highest level of overall shear rate stress among all agitation methods.

3.3.3. *System maximum shear rate*

Table 2(a) lists the system maximum shear rate at the highest agitation frequencies. For system maximum shear rate, the rank ordering of agitation methods is: vortex mixer > magnetic stirrer > orbital shaker > rotator. Any of these maximum shear rate values is much lower than those generated by the viscometer, capillary tube or rheometer devices in the literature, which range from 20,000 to 100,000 s^{-1} (Thomas and Dunnill, 1979; Virkar et al., 1981; Jaspe and Hagen, 2006; Bee et al., 2009a). They are also all well below the shear rates of 10^7–10^8 s^{-1} that have been predicted to be theoretically capable of unfolding proteins by correlation of shear forces with those necessary to unfold proteins in atomic force microscope (AFM) experimental studies (Bee et al., 2009b), or using computational simulations of the impact of shear on protein folding (Alexander-Katz and Netz, 2008).

3.3.4. *Total shear*

One frequently listed shear parameter in the literature is total shear, which takes into account the shear rate and the time of exposure (Virkar et al., 1981; Maa and Hsu, 1997; Bee et al., 2009a,b). This term may be relevant if the denaturation process is gradual and requires a persistent stress, or if the process is quick and degradant accumulates linearly over time. It may also be relevant in describing particle size distributions that are affected by orthokinetic flocculation and disintegration under shear. Table 2(a) lists the values of total shear calculated based on the system volume averaged shear rates and 24 h of agitation time at highest agitation frequencies covered in this work for each of the agitation method. The vortex mixer at 1000 rpm produces highest value of system total shear over 24 h of agitation time. The total shear generated by vortex mixer and magnetic stirrer are comparable to the total shear values described in published studies (Thomas and Dunnill, 1979; Virkar et al., 1981), which range from 10^7 to 5×10^8. However, these values of total

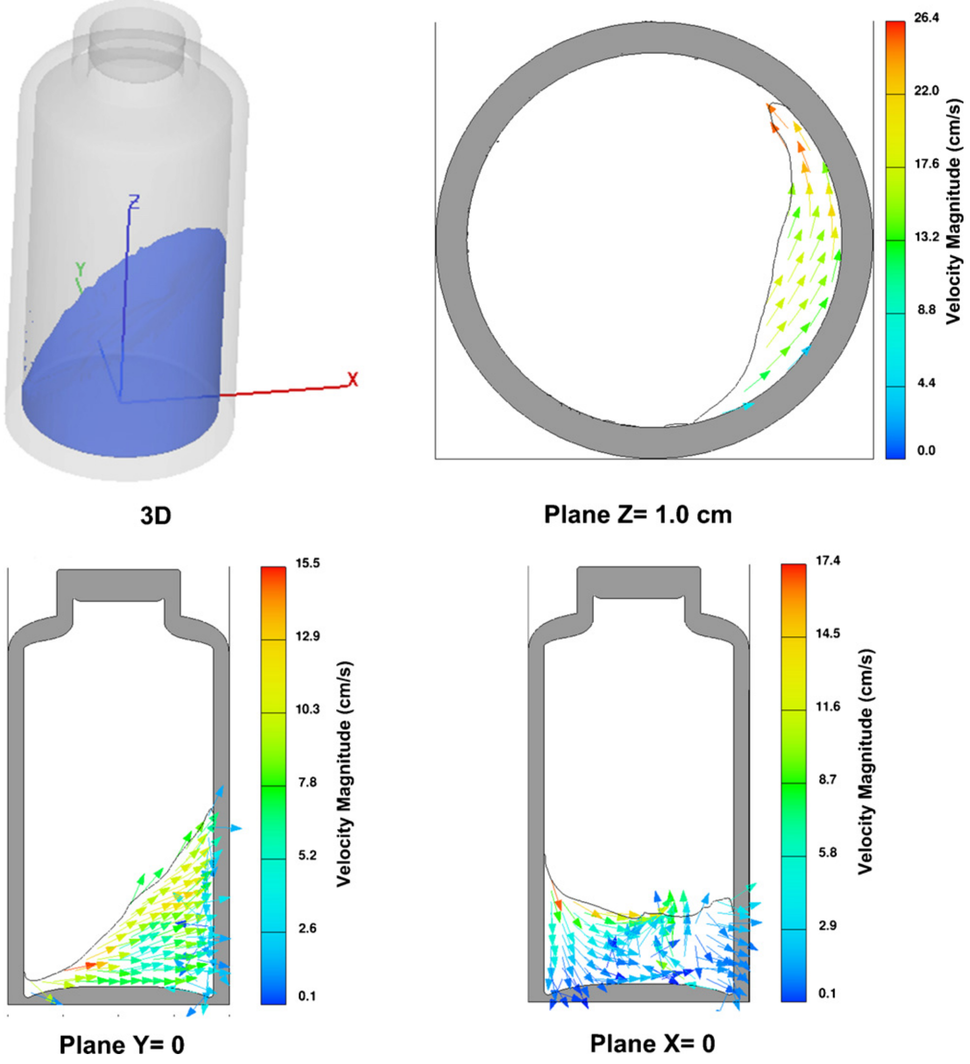

Fig. 6. Flow patterns of the orbital shaker at 300 rpm at steady state (cm s^{-1}).

shear were generated by a viscometer with a much smaller volume of liquid, higher average shear rates, and within much shorter amount of time. Thus, the majority of the conditions covered in this work at lower frequencies result in much less total shear even after 24 h agitation. Even if the total shear were made equal by extending the time, it may not be universally true that a low shear rate compounded over a long time generates an equivalent product quality impact as an intense shear incurred over a short time.

3.4. *Air–liquid interfacial stresses*

3.4.1. *Area of the air–liquid interface*

Fig. 10(a) shows a comparison of the area of air–liquid interface among agitation methods at different agitation frequencies. The area of air–liquid interface is normalized against its value when there is no motion of the fluid (1.67 cm^2). In general, for all agitation methods, an increase in agitation frequency results in an increase of the air–liquid interfacial area. The vortex mixer generates a vertically and horizontally elongated air–liquid interface (Fig. 7) with much more air–liquid interfacial area compared to the other three agitation methods at any agitation frequency. The next highest value corresponds to the orbital shaker at 300 rpm. Considering its very low agitation frequencies, the rotator generates significant amount of air–liquid interface. As the vial rotates, the air–water surface alternately spans the circular cross section when the vial is upright and the longer, approximately rectangular, cross section when the vial is horizontal, thus undergoing cyclical expansion and contraction (Fig. 3(b)). At 10 rpm, the rotator creates more air–liquid interface than the orbital shaker at 200 rpm or the magnetic stirrer at 1000 rpm. The magnetic stirrer is the least effective at creating air–liquid interfacial area. Generally, one might expect an increase in interfacial damage of proteins when the air–water interfacial area increases. However, the relative activity of these interfaces may depend on other fluid flow characteristics such as convection, shear and dilatation.

Besides the air–liquid interface at the fluid free surface, air bubbles entrained into the bulk fluid due to agitation can also create air–liquid interfaces. Although Flow-3D® has a built-in model to simulate the formation of air bubbles, accurate capturing of the air–liquid interface created by these air bubbles requires a mesh cell size much smaller than the actual bubble size, which requires extensive computational resources not practically achievable. Thus, air–liquid interfaces present due to air bubble trapping were left out of the scope of this work but the authors note that there is the possibility that they also have an additional impact on protein degradation. The area of air–liquid interface presented in this work for all agitation methods could have been under-estimated due to this reason. Among the four agitation methods, the highest degree of under-estimation on area of air–liquid interface could belong to vortex mixer since the agitation of vortex mixer is the most

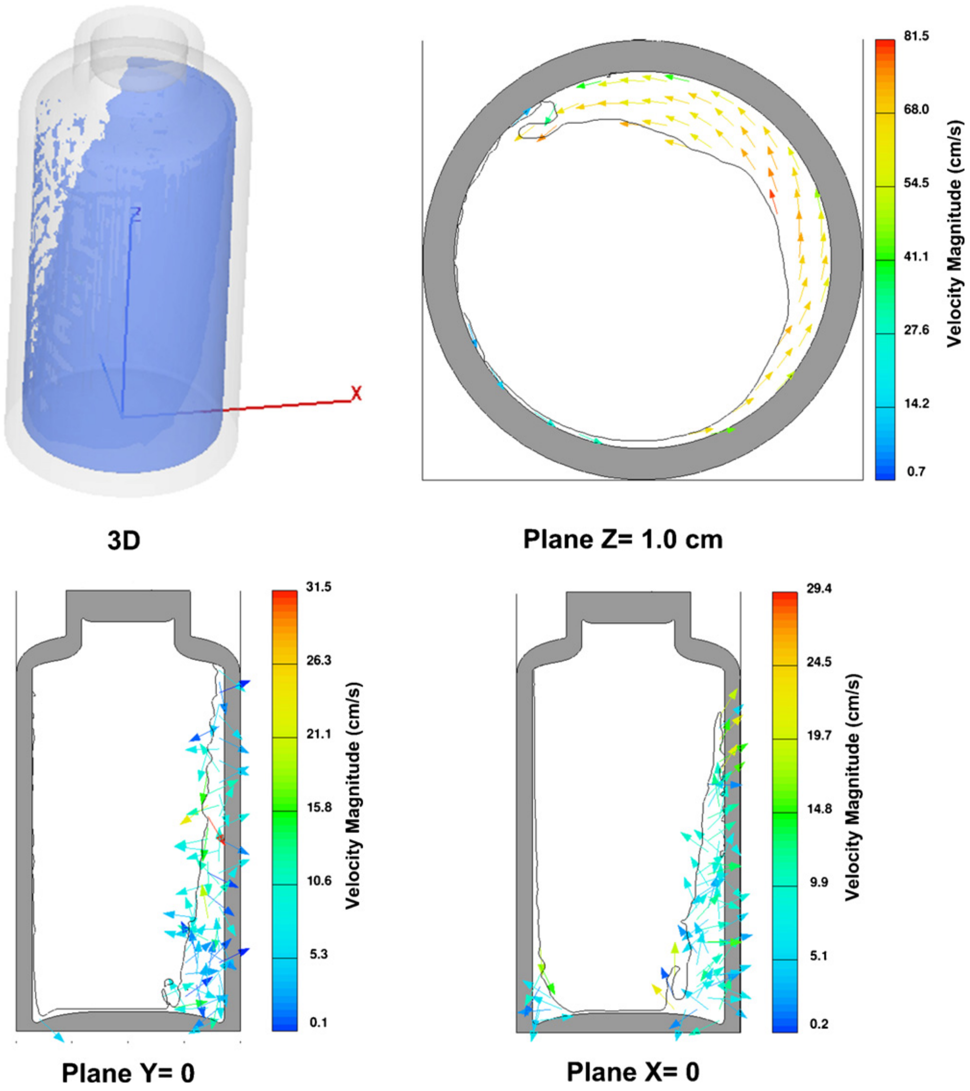

Fig. 7. Flow patterns of the vortex mixer at 1000 rpm at steady state (cm s^{-1}).

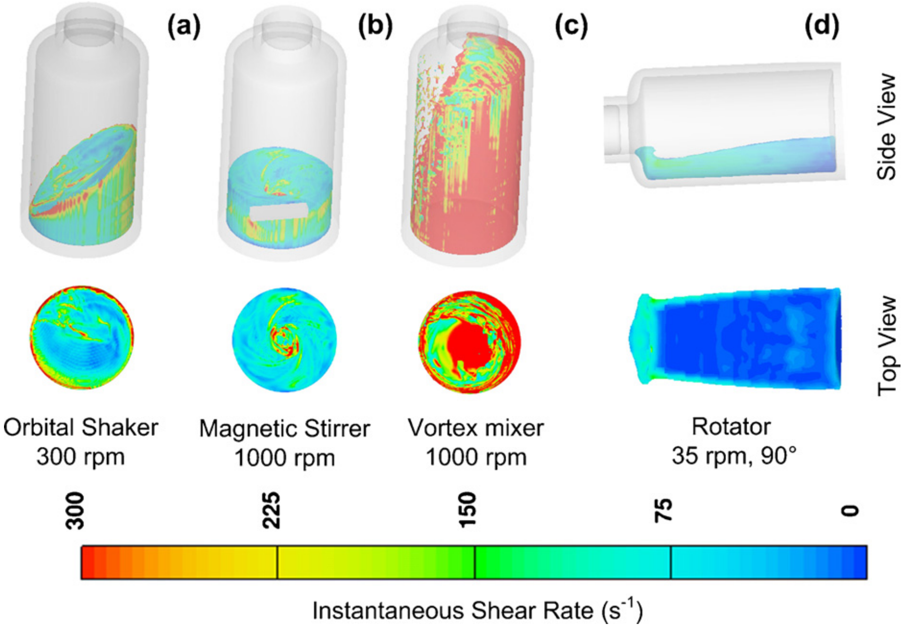

Fig. 8. Instantaneous shear rates in the mesh cells near interfaces: (a) orbital shaker at 300 rpm, (b) magnetic stirrer at 1000 rpm, (c) vortex mixer at 1000 rpm and (d) rotator at 35 rpm. (For interpretation of the references to color in the text, the reader is referred to the web version of this article.)

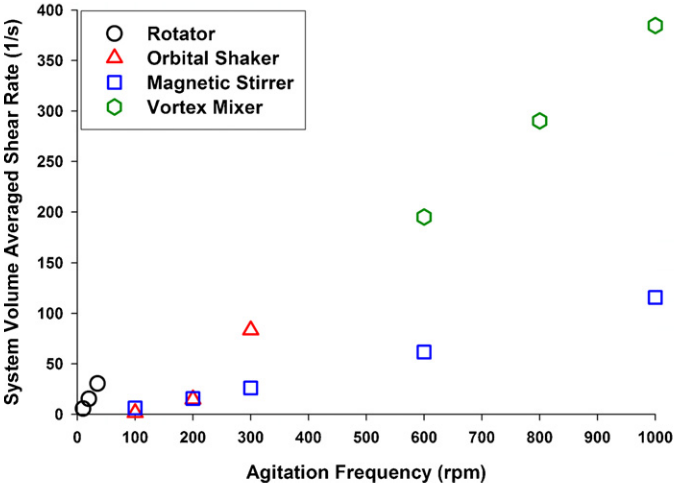

Fig. 9. Comparison of the system volume averaged shear rates.

vigorous under same agitation frequency thus could entrap the highest amount of air bubbles in the bulk fluid. The underestimation of the air–liquid interface created by air bubble could also have impact on the calculation of shear rate near air–liquid interface and air–liquid interface regeneration but the exact impact is unknown at this point.

3.4.2. *Volume averaged shear near air–liquid interface*

Fig. 10(b) shows the dependence of $\dot{\gamma}_{A-L}$ on frequency. $\dot{\gamma}_{A-L}$ increases approximately linearly with agitation frequency for most of the agitation methods. Again, and inflection can be seen in the trend for the orbital shaker as the fluid body becomes elongated at frequencies above 200 rpm. For the rotator, there is a steep increase in shear rate from 10 rpm to 35 rpm, perhaps due to the increased velocity of the fluid flowing from end-to-end and the resulting greater splash on impact at the vial top and bottom. The magnetic stirrer generates lower $\dot{\gamma}_{A-L}$ compared to orbital shaker and vortex mixer at the same agitation frequencies. At the maximum operating speeds simulated, the rank ordering of equipment with respect to $\dot{\gamma}_{A-L}$ is: vortex mixer ≫ orbital shaker > magnetic stirrer > rotator (Table 2(b)). Air–liquid interface and shear rate near this interface are thought to act cooperatively to unfold and/or aggregate proteins (Maa and Hsu, 1997; Colombié et al., 2001; Chou et al., 2005; Mahler et al., 2005; Bee et al., 2009a; Thomas and Geer, 2011). However, the degree of the contribution from each of the two individual components of the shear rate/air–liquid interface on protein aggregation is currently unknown. The synergetic effect may be drug and formulation dependent. Adsorbed proteins may aggregate to form networks resulting in a gel layer at the air–liquid interface (Petkov et al., 2000; Murray et al., 2002). Shear may disrupt the surface gel layer and may produce different types and sizes of aggregates or particles for constantly agitated systems versus periodically agitated systems (Van Aken and Merks, 1996).

3.4.3. *Maximum shear rate near air–liquid interface*

At the maximum operating frequencies simulated, the rank ordering of equipment with respect to $\dot{\gamma}_{A-L}^{\max}$, is: vortex mixer ≫ orbital shaker > magnetic stirrer > rotator (Table 2(b)). All these values are smaller than the $\dot{\gamma}_{sys}$ shown in Table 2(a), indicating the maximum shear rates do not appear near the air–liquid interface for any of the four agitation methods. However, the disruptive impact on protein stability may be enhanced by the interface (e.g. due to its hydrophobic and fluid nature), even if the shear forces are insufficient alone.

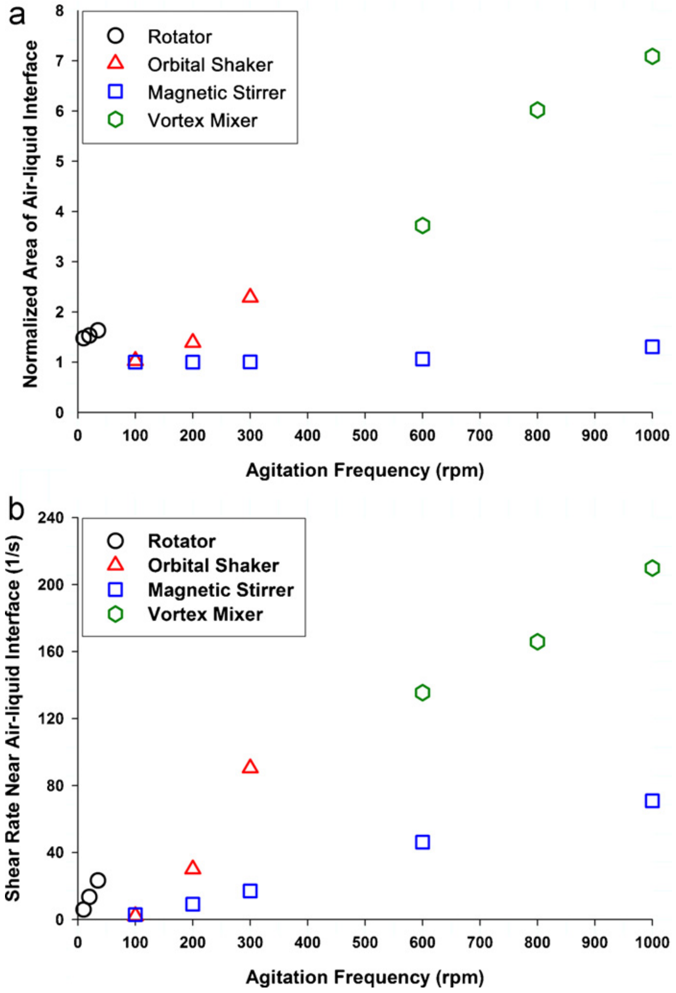

Fig. 10. Comparisons of areas of air–liquid interfaces and volume averaged shear rate near the air–liquid interfaces.

3.4.4. *Air–liquid interface regeneration rate*

In many instances surface-induced aggregation may be surface area limited. For instance, aggregation of a mAb at the stainless steel surface had a second-order dependence on steel surface area (Bee et al., 2010b). Similarly, if protein aggregation is limited by available free air–liquid interfacial area, or the available surface is crowded with protein, then creation of fresh interface should increase the overall aggregation rate. The air–liquid interface is unique in that it is fluid in nature, and can be deformed, regenerated, or turned over by relatively gentle fluid forces.

Fig. 11 shows the dependence of *G* on agitation frequency for the four instruments. Even at the lowest agitation frequency setting, the vortex mixer regenerates more air–liquid interface per time than all other methods at any frequency. At an agitation frequency of 1000 rpm, its air–liquid interface regeneration rate climbs up to 2.34 mL s^{-1}. The air–liquid interface regeneration rate for the rotator increases steeply with frequency too in an approximately linear manner. Even though it is limited to low frequency, it has a comparable surface regeneration rate to the magnetic stirrer and orbital shaker at their higher frequency settings. The relatively low surface generation rate for the magnetic stirrer is perhaps surprising. In many processes, stirrers are used to effectively mix fluids, even in deep tanks. The secondary rolling convective currents in the vertical planes (shown in Fig. 5) might be assumed to create significant convective turnover at the surface, but these simulations show that the effect is small compared to the mechanisms for creating surface

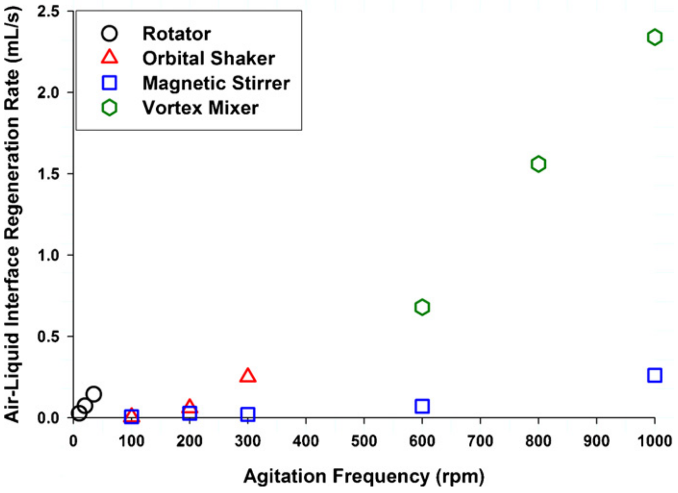

Fig. 11. Comparison of the air–liquid interface regeneration rates.

turnover in the other agitation methods at the frequencies modeled. At the maximum agitation frequencies simulated, the rank ordering of equipment with respect to cumulative air–water surface regeneration rate is: vortex mixer ≫ magnetic stirrer > orbital shaker > rotator (Table 2(b)).

Fig. 12 shows color maps of the air–liquid interface generation rates, G_c, for agitation methods at their highest agitation frequencies at steady state. The vast difference in cumulative regeneration, G, incurred in the vortex system versus the other three methods is difficult to discern from these color maps. This is perhaps due to the line of sight passing tangentially across the large, mostly vertical, liquid layer dispersed against the vial wall. It is clear that regeneration is intense in small regions of the surface for the vortex mixer and magnetic stirrer. The entire surface is much more quiescent for the orbital shaker and rotator, at the rotation angle shown here. Comparison of the surface shear maps (Fig. 8) with the regeneration rate map here demonstrates that in many cases they coincide, for example in the top end of the vial on the rotator, and in the central region for the magnetic stirrer.

To roughly estimate how the volumetric term G (mL s^{-1}) translates into air–liquid interface area generation (cm^2/s), the surface fluid volume can be visualized as occupying the surface fluid layer mesh cells, which are only partially filled with fluid, and the fluid depth in this work is less than 170 μm. Approximating the surface depth is 100 μm everywhere, the maximum G in this study provided by vortex mixer at 1000 rpm (2.34 mL s^{-1}) is equivalent to 234 cm^2 of newly created surface with a depth of 100 μm, generated every second. Though these assumptions enable only a rough estimate, compared to the area of air–liquid interface at rest in these system (1.67 cm^2), it is clear that the surface turns over rapidly, on the order of hundreds of times per second. From surface tension experiments, it is known that adsorption of proteins to interfaces and formation of gel layers at a surface can take hundreds of minutes to equilibrate (Tripp et al., 1995; Murray et al., 2002; Ridout et al., 2004). Thus the short lifetime of the surface in the vortex system here would presumably limit the types of aggregates ultimately formed to those that result from relatively quick surface processes. None of the systems here would be likely to facilitate surface processes that take more than a few seconds.

Even when air–liquid interface is available for protein adsorption, the supply of fresh fluid from the bulk to the surface may be limiting. Table 2(b) provides the comparison of liquid recirculation intensity, n, among the agitation methods under their highest agitation frequencies for 24 h of agitation. Fluid agitated with the vortex mixer has the highest recirculation intensity, thus increasing the chance for protein molecules from the bulk to participate in surface reactions. The rotator has the lowest recirculation and therefore is least capable to circulate drug from the bulk to the air–liquid interface.

3.5. *Solid–liquid interfacial stresses*

3.5.1. *Area of solid–liquid interface*

Fig. 13(a) shows the comparison of the solid–liquid interfacial area among agitation methods at different agitation frequencies. The interfacial area is normalized against its value under static conditions (4.77 cm^2 for magnetic stirrer and 4.74 cm^2 for others). The solid–liquid interfaces shown in this figure include the glass–water interface for all agitation methods and also the stopper–water interface for the rotator only. For all other three agitation methods, the fluid does not touch the stopper even at the highest modeled agitation frequencies. The general trend is similar to the air–liquid interface trends in Fig. 10(a). For all agitation methods, the solid–liquid interface increases with agitation frequency. The vortex mixer generates much more solid–liquid interface compared to other agitation methods with the normalized area of solid–liquid interface almost tripling at the higher frequencies. The smallest increases in interfacial area are seen with the rotator and magnetic stirrer.

There is an extra solid–liquid interface in the magnetic stirrer system which is located at the magnetic stir bar surface. The area of this interface is 0.43 cm^2 when there is no fluid motion, and it does not change due to the increase of agitation frequency. The shear rate is high in the region near the stir bar, and in addition, the unique stir bar surface properties may play an important role in protein degradation. The most commonly used magnetic stir bars in biopharmaceutical development laboratories are Teflon® coated, and therefore present a hydrophobic surface which could contribute significantly to protein aggregation (Colombié et al., 2001). However, it was also reported that some proteins do bind to hydrophilic surfaces and aggregate more than on hydrophobic surfaces (Haynes and Norde, 1994). The preferences of surface properties in terms of protein binding and aggregation are probably protein and formulation dependent. All results for the magnetic stirrer system presented in this work are based on a particular type and size of magnetic stir bar. The size and shape of magnetic stir bar have a significant impact on the behavior of stirred fluid. This fact actually provides flexibility to the magnetic stirrer system to generate different levels of stresses. The behavior of stirred fluid with a large or unique shape of stir bar can be numerically simulated by CFD with the same approach presented here to target specific fluid stresses and intensities.

The roughness of a solid surface greatly impacts the net area, but surface roughness is difficult to capture in simulations. The solid–liquid interfacial areas in these simulations were calculated by assuming a perfectly smooth surface. Protein aggregation was found to be directly proportional to solid surface roughness under constant shear rate in one study (Biddlecombe et al., 2009). Thus the experimentalist should consider the surface roughness along with other properties of the solid surfaces when designing experiments and interpreting results.

3.5.2. *Volume averaged shear near the solid–liquid interface*

Fig. 13(b) shows a comparison of the volume averaged shear rate near the solid–liquid interface, $\dot{\gamma}_{S-L}$, among the four agitation methods at different agitation frequencies. The $\dot{\gamma}_{S-L}$ increases with agitation frequency and the general trend of data is very similar to the $\dot{\gamma}_{A-L}$ dependency (Fig. 10(b)). However, the shear rates near the solid–liquid interfaces are generally greater than those at the air–liquid interfaces. Again, the vortex mixer generates the highest shear among the four instruments. And again, the shear

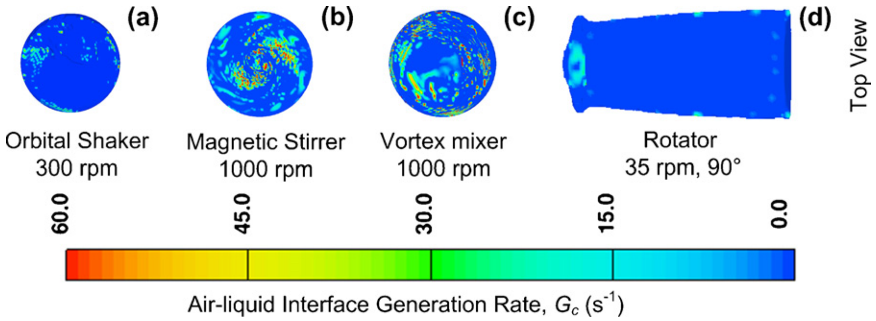

Fig. 12. Air–liquid interface generation rates, G_c, top view.

rate increases abruptly for orbital shaker as the agitation frequency increases from 200 to 300 rpm, in parallel with the vertical elongation of the fluid body.

3.5.3. *Volume averaged shear rate near the magnetic stir bar surface*

The volume averaged shear rate near the magnetic stir bar surface is shown in Fig. 14 and compared with the other volume averaged shear rates in the system. The shear rate near the stir bar increases approximately linearly with agitation frequency up to 1000 rpm. At any given agitation frequency, the shear near the stir bar surface interface is at least 2.5 times higher than any other volume averaged shear rate values shown in the same figure. The system volume averaged shear rates are higher than those near air–liquid interface and solid–liquid interface at the vial glass. The very high shear rate near stir bar seems to weigh significantly in the system volume averaged shear rate since the area of air–liquid interface (1.67 cm^2) and the area of the glass-liquid interface (4.77 cm^2) are much larger than the area of the stir bar surface (0.43 cm^2). The magnetic stir bar is the major source of shear rate in the magnetic stirrer agitation system. This high shear rate combined with the hydrophobic Teflon® surface may be the major cause of protein aggregation in the magnetic stirrer system (Kiese et al., 2008).

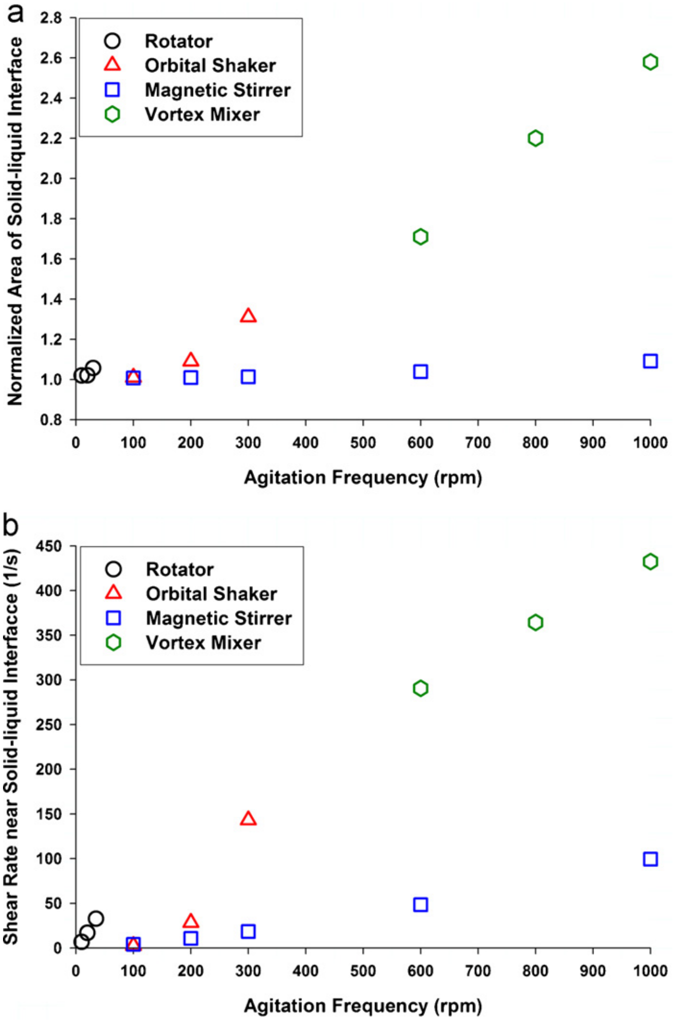

Fig. 13. Comparisons of the solid–liquid interfacial areas and volume averaged shear rate near the solid–liquid interfaces.

3.5.4. *Maximum shear rate near solid–liquid interface*

At the maximum operating frequencies simulated, the rank ordering of equipment with respect to, $\dot{\gamma}_{S-L}^{\max}$ is: vortex mixer > magnetic stirrer > orbital shaker > rotator (Table 2(b)). All these values are smaller than the $\dot{\gamma}_{sys}$ shown in Table 2(a), indicating the maximum shear rates do not appear near solid–liquid interfaces for any of agitation methods, with one exception. The maximum shear rate near the solid–liquid interface at the stir bar surface is the maximum shear rate for the magnetic stirrer system.

3.6. *Cavitation potential*

Within the scope of this work, cavitation potential was not observed in fluid agitated with any of the instruments up to 1000 rpm.

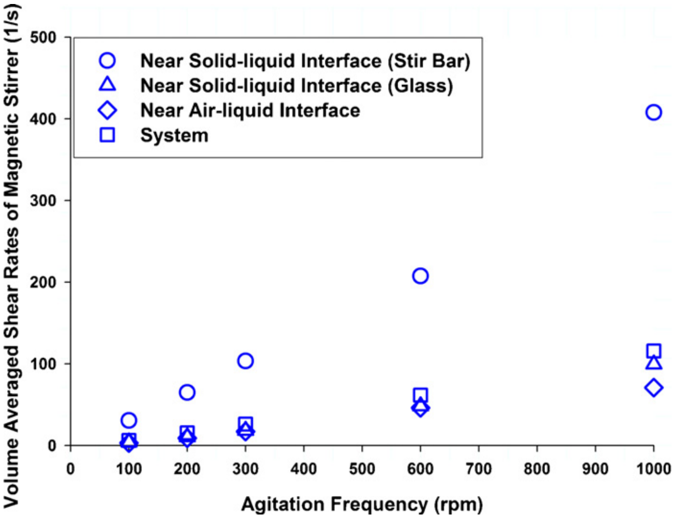

Fig. 14. Comparison of shear rates for the magnetic stirrer.

3.7. Other considerations for vial agitation

The fluid in a rotating vial has contact with two types of solid–liquid interfaces: glass–liquid and stopper–liquid. Some stoppers have a silicone oil coating for fill finish machinability and reduced friction on insertion into the glass vial. The presence of the stopper–liquid interface together with the shear rate near this interface could potentially lead to emulsification of small silicone oil droplets into the bulk liquid and cause protein aggregation (Jones et al., 2005; Thirumangalathu et al., 2009). It may be wise to choose a stopper that is not siliconized when agitating a vial with rotator to eliminate this additional stress. Silicone oil is not as likely to be emulsified for the other three agitation methods because based on visual observations and the CFD simulation results, agitated fluids do not reach the stopper even at the highest frequencies.

Although the orbital shaker generates lower stresses than the vortex mixer, it has an advantage. The agitation platform of orbital shaker is much larger and more stable than that of the vortex mixer. It can hold and agitate multiple vials simultaneously without adding any accessories and can maintain the same strict orbital motion for every vial. This is very helpful in eliminating sample to sample variability. The vortex mixer requires accessories (e.g. vial holders) to be used to agitate multiple vials at the same time. When this accessory is used, the weight of the vials plus the weight of the accessory may disturb the motion of the agitation head of the vortex mixer. It can be observed often that the motions of vials are no longer strictly orbital. Also, there could be variability in the motion experienced by different vials. It is difficult to use CFD to simulate the irregular orbital motions of vials since the motion parameters are unknown.

One observation from vial agitation experiments is that a thin layer of fluid can adhere to glass surfaces (and stopper surfaces in the case of the rotator) after contact by the bulk agitated fluid. The thin layer of adhered fluid on these surfaces creates both solid–liquid and air–liquid interfaces. This thin layer of fluid persists until the bulk fluid returns and brings fresh fluid to displace the old layer, and then presumably the adhered layer is refreshed with new material. This adhered layer can be observed mainly with the rotator, orbital shaker and vortex mixer. For the magnetic stirrer, there is almost no thin layer of liquid observed due to the dispersion of fluid symmetrically around the vial wall, and the relatively low glass solid–liquid interface overall. At lower agitation frequencies, the adhesion interfaces can exist for longer periods before being brought back into contact with the bulk fluid, which provides more time for protein aggregation to occur at these interfaces. The aggregated protein on these adhesion interfaces may be brought back into the bulk fluid, or perhaps denatured proteins introduced into the bulk to serve as nuclei for aggregation. In spite of the possibility of aggregation resulting from these adhered layers, they could not be taken into account in this work due to the current limitations of the simulation software. On top of all stresses covered in this work, when using a rotator, orbital shaker, or vortex mixer to agitate a protein solution, the stress factors incurred in adhered liquid layers need to be considered when designing experiments and interpreting experimental results.

A large portion of our current understanding of protein behavior at air–water interfaces comes from the fields of food, colloid, and interfacial sciences (Freer et al., 2004; Ridout et al., 2004; Martin et al., 2005). In particular, interfacial rheology experiments have been effective at elucidating fundamental insights into the kinetics of protein adsorption, unfolding and cohesive bonding of proteins in adsorbed layers, formation of gel-like layers, and the resulting impact on surface tension, elasticity and viscosity. Thus one may wish to apply these fundamental findings directly in simulations to make predictions from first principles, but some difficulties still remain. Two phenomena are routinely probed in surface rheology experiments, surface shear deformation and dilatational deformation. In surface shear deformation, the surface deforms without changing in area (e.g. fluid is filled between concentric cylinders that rotate in opposite directions, shearing the interface in between), and the velocity gradient is considered only in the interfacial plane. This in-plane interfacial shear cannot be modeled currently using the Flow-3D® software, but rather the 3-dimensional velocity gradients in the mesh cell at the surface are used to calculate the shear rate “near the interface”. In dilatational (same word origin as dilation) deformation, the surface expands while maintaining constant shape, as in a Langmuir trough or drop tensiometer with a growing droplet. The related concept used in these simulations is surface generation. A key difference is that unlike fundamental experiments where dilatational deformation is isolated, it is accompanied by shear and convection in an agitated system, and further, dilatation in one area may be accompanied by surface compression in a neighboring area, creating non-uniform surface deformations. The age of specific locations on the surface is also not tracked with the current software thus preventing time-dependent surface properties like surface tension or surface viscosity from being mapped onto the surface. In spite of these current limitations, CFD modeling of agitation methods helps to make approximate comparisons and to put the two systems in perspective relative to one another. For example, surface rheology experiments study the variation of surface properties over logarithmic time scales, and CFD simulations allow one to estimate that the relevant processes are on the millisecond–second time scale, not hours. Aggregation may still result from processes at these time scales, but the mechanistic explanation (e.g. conformational changes or collision frequency increase due to mixing) should be consistent with the expected time scales.

3.8. Possible improvements in protein agitation study design using CFD simulation results

The analyses covered in this work highlight the inherent complexity involved in the rational design of laboratory agitation studies to model stresses incurred under “real world” conditions. The “real world” conditions likely are even more complicated. For formulation scientists, in order to develop a reliable formulation to protect the stability of protein medicine, it is critical to identify specific stress(es) problematic for each protein, which could be air–liquid interface plus shear, or solid-interface plus shear or even a Teflon surface of the magnetic stir bar by itself. Even if detailed CFD characterizations were easily obtained for any scenario where agitation is incurred, it would still probably be impossible to match the intensity of all “real world” stresses perfectly in a single laboratory model. However, the goal of agitation studies is usually to assure stability under “real world” conditions, not to model the anticipated stresses exactly. So verification that the laboratory model is indeed “worst-case” by CFD is a valuable exercise. The work described here provides the laboratory half of the analysis for several common agitation methods using a particular container, fill volume and fluid, and the remaining “real world” half of the analysis remains to be done and would be tailored to the anticipated shipping or processing scenario. Thus for those who aim to qualitatively or quantitatively compare laboratory agitation methods to anticipated stresses, publication of further CFD studies of common biotechnology processes and shipping stresses would be valuable as most of the “real world” stresses are hard to measure with experimental methods too.

In practice, the fluid properties of protein solutions (e.g. viscosity) can vary from product to product depending on the molecular weight and concentration of protein, and types and concentrations of excipients. Further, container size and fill volumes vary widely. It would be impossible to conduct CFD simulations to guide agitation study design for every individual protein solution in every presentation, shipping route and process, and so as a practical matter, generalizations must be drawn from a limited number of simulations. As an example, the rank ordering of stresses in this work were calculated for 1 mL of water at 25 °C in a 3 mL glass vial, but a similar rank ordering of stresses might be reasonably expected for 1.2 mL of a low concentration monoclonal antibody formulated with low molecular weight excipients in a similar vial. Even if the antibody had a concentration above 100 mg/mL, and the viscosity were much higher than water, it can be reasonably expected that stirring would still impart a high shear at the stir bar solid–liquid interface, vortex mixing would disperse the liquid to the greatest height on the vial wall, and rotation would still produce a high surface turnover relative to its slower frequency. The effects of variables suspected to play an important role, such as viscosity and fill volume, should be assessed in separate CFD studies to better understand their impact and guide CFD-derived interpretations. The same issues exist when applying platform agitation study designs across multiple biotechnology products, formulations, or fill volumes, but without CFD as a guide the stresses are unlikely to be fully understood.

Tailoring agitation studies for specific proteins might require identification of the particular stresses that are most damaging on a protein-by-protein basis, and experiments could then be prioritized according to stress type and intensity using a risk-based approach. Based on the results shown in this work, it is clear that each of the most commonly used laboratory agitation methods provide several agitation mechanical stresses simultaneously and different agitation methods provide different types and intensities of stresses under same agitation frequencies. To use these methods as they are with a randomly picked agitation frequency may result in degradation of a protein. However, such an experiment may not be very helpful in understanding the real mechanism(s) behind the problem(s) since it is difficult to de-convolute the many involved factors to identify the root cause(s). A simpler analysis might result from using agitation methods targeting specific types of stresses with reasonably defined and controlled intensities. For example, one can fill the glass vial full to eliminate the air–liquid interface in stirring studies, rotate vials with a low speed and long interval to minimize the shear rate while maintain high air–liquid interface turnover. With isolated agitation stresses provided by well designed agitation experiments, the mechanism(s) of protein aggregation can be identified and understood. CFD can aid in the design and validation of targeted stress methods.

4. Conclusions

In this study, agitation experiments involving 1 mL of fluid in a glass vial agitated by four different types of common lab agitation methods were modeled at various agitation frequencies. Fluid stresses in the bulk liquid and near air–liquid and solid–liquid interfaces were found to be variable among the different methods and often strong functions of agitation frequency. Average and maximum shear rates were found to be well below the levels that many authors have predicted to be necessary to directly unfold proteins, but may be important from the standpoint of particle flocculation and disintegration or synergetic effects of interfacial adsorption and unfolding combined with shear and turnover at the air–water interface. Overall, the shear rates were highest for the vortex mixer. High air–liquid interfacial shear rates coincided with high turnover rates, and average surface shear and net surface turnover was by far the highest for the vortex mixer. The magnetic stirrer generated relatively high shear near the stir bar solid–liquid interface. The combination of high shear and the hydrophobic surface makes the stir bar surface a suspect source of aggregates for this system. The rotator provides a relatively large amount of shear and interfacial area considering the very low agitation frequency. Cavitation potential was not seen for any of the agitation methods in the frequency ranges studied in this work. Selection of the proper agitation method with known types and intensities of stresses can facilitate better understanding of protein degradation mechanisms. CFD can be instrumental in characterizing fluid stresses in experimental systems and in validating their relevance to “real world” conditions.

Acknowledgments

The authors would like to thank Steven Bishop and Stephen Chang for their support and encouragement. Michael Barkhudarov, Jeff Burnham, Melissa Carter, John Ditter and Joel Jacob of Flow Science Inc. are acknowledged for support and discussions on Flow-3D® software.

References

Akiti, O., Yeboah, A., Bai, G., Armenante, P.M., 2005. Hydrodynamic effects on mixing and competitive reactions in the laboratory reactors. Chem. Eng. Sci. 60, 2341–2354.

Alexander-Katz, A., Netz, R.R., 2008. Dynamics and instabilities of collapsed polymers in shear flow. Macromolecules 41, 3363–3374.

Alexeenko, A., Ganguly, A., Nail, S., 2009. Computational analysis of fluid dynamics in pharmaceutical freeze-drying. J. Pharm. Sci. 98, 3483–3494.

Anderson, D.A., Tannehill, J.C., Pletcher, R.H., 1984. Computational Fluid Mechanics and Heat Transfer. McGraw-Hill, New York.

Bai, G., Armenante, P.M., 2008. Velocity distribution and shear rate variability resulting from changes in the impeller location in the USP dissolution testing apparatus II. Pharm. Res. 25, 320–336.

Bai, G., Armenante, P.M., 2009. Hydrodynamic, mass transfer, and dissolution effects induced by tablet location during dissolution testing. J. Pharm. Sci. 98, 1511–1531.

Bai, G., Armenante, P.M., Plank, R.V., 2007a. Experimental and computational determination of blend time in USP dissolution testing apparatus II. J. Pharm. Sci. 96, 3072–3086.

Bai, G., Armenante, P.M., Plank, R.V., Gentzler, M., Ford, K., Harmon, P., 2007b. Hydrodynamics investigation of USP dissolution test apparatus II. J. Pharm. Sci. 96, 2327–2349.

Bai, G., Wang, Y., Armenante, P.M., 2011. Velocity profiles and shear strain rate variability in the USP Dissolution Testing Apparatus 2 at different impeller agitation speeds. Int. J. Pharm. 403, 1–14.

Barkhudarov, M.R., 2004. Multi-block gridding technique for Flow-3D®. Flow Science Technical Note #59.

Becker, G.W., Bowsher, R.R., Mackellar, W.C., Poor, M.L., Tackitt, P.M., Riggin, R.M., 1987. Chemical, physical, and biological characterization of a dimeric form of biosynthetic human growth hormone. Biotechnol. Appl. Biochem. 9, 478–487.

Bee, J.S., Stevenson, J.L., Mehta, B., Svitel, B., Pollastrini, J., Platz, R., Freund, E., Carpenter, J.F., Randolph, T.W., 2009a. Response of a concentrated monoclonal antibody formulation to high shear. Biotechnol. Bioeng. 103, 936–943.

Bee, J.S., Chiu, D., Sawicki, S., Stevenson, J.L., Chatterjee, K., Freund, E., Carpenter, J.F., Randolph, T.W., 2009b. Monoclonal antibody interactions with micro- and nanoparticles: adsorption, aggregation, and accelerated stress studies. J. Pharm. Sci. 98, 3218–3238.

Bee, J.S., Schwartz, D.K., Freund, E., Carpenter, J.F., Randolph, T.W., 2010a. ‘DO NOT SHAKE’: protein particle formation caused by compression of the air–water interface. In: AAPS Workshop on Protein Aggregation and Immunogenicity, Breckenridge, CO.

Bee, J.S., Davis, M., Freund, E., Carpenter, J.F., Randolph, T.W., 2010b. Aggregation of a monoclonal antibody induced by adsorption to stainless steel. Biotechnol. Bioeng. 105, 121–129.

Bee, J.S., Randolph, T.W., Carpenter, J.F., m Bishop, S.M., Dimitrova, M.N., 2011. Effects of surfaces and leachables on the stability of biopharmaceuticals. J. Pharm. Sci., doi:10.1002/jps.22597.

Biddlecombe, G.J., Craig, V.A., Zhang, H., Yddin, S., Mulot, S., Fish, C.B., Bracewell, G.D., 2007. Determining antibody stability: creation of solid–liquid interfacial effect within a high shear environment. Biotechnol. Prog. 23, 1218–1222.

Biddlecombe, G.J., Smith, G., Uddin, S., Mulot, S., Spencer, D., Gee, C., Fish, C.B., Bracewell, G.D., 2009. Factors influencing antibody stability at solid–liquid interfaces in a high shear environment. Biotechnol. Prog. 25, 1499–1507.

Bird, R.B., Stewart, E.W., Lightfoot, N.F., 2002. Transport Phenomena. John Wiley & Sons, Inc., New York.

Branden, C., Tooze, J., 1998. Introduction to Protein Structure, second ed. Garland Science, New York.

Brych, S.R., Gokarn, Y.R., Hultgen, H., Stevenson, R.J., Rajan, R., Matsumura, M., 2010. Characterization of antibody aggregation: role of buried, unpaired cysteines in particle formation. J. Pharm. Sci. 99, 764–781.

Byron, W.F., Fuller, W.R., 1992. Mathematics of Classical and Quantum Physics. Dover Publications, New York.

Chou, D.K., Krishnamurthy, R., Randolph, T.W., Carpenter, J.F., Manning, M.C., 2005. Effects of Tween 20® and Tween 80® on the stability of Albutropin during agitation. J. Pharm. Sci. 94 (6), 1368–1381.

Colombié, S., Gaunand, A., Lindet, B., 2001. Lysozyme inactivation under mechanical stirring: Effect of physical and molecular interfaces. Enzyme. Microb. Tech. 28 (9–10), 820–826.

Cromwell, E.M.M., Hilario, E., Jacobson, F., 2006. Protein aggregation and bioprocessing. AAPS J. 8, 572–579.

Eppler, A., Weigandt, M., Hanefeld, A., Bunjes, H., 2010. Relevant shaking stress conditions for antibody preformulation development. Eur. J. Pharm. Biopharm. 74, 139–147.

Freer, E.M., Yim, K.S., Fuller, G.G., Radke, C.J., 2004. Interfacial rheology of globular and flexible proteins at the hexadecane/water interface: comparison of shear and dilatation deformation. J. Phys. Chem. B 108, 3835–3844.

Gulseren, I., Guzey, D., Bruce, B.D., Weiss, J., 2007. Structural and functional changes in ultrasonicated bovine serum albumin solutions. Ultrason. Sonochem. 14, 173–183.

Harrison, R.G., Todd, P.W., Rudge, S.R., Petrides, D., 2003. Bioseparations Science and Engineering. Oxford University Press, New York.

Haynes, C.A., Norde, W., 1994. Globular proteins at solid/liquid interfaces. Colloids Surf. B 2, 517–566.

Hirt, C.W., Nichols, B.D., 1981. Volume of fluid (VOF) method for the dynamics of free boundaries. J. Comput. Phys. 39, 201–225.

Jaspe, J., Hagen, S.J., 2006. Do protein molecules unfold in a simple shear flow? Biophys. J. 91 (9), 3415–3424.

Katakam, M., Banga, A.K., 1997. Use of poloxamer polymers to stabilize recombinant human growth hormone against various processing stresses. Pharm. Dev. Technol. 2, 143–149.

Jones, L.S., Kaufmann, A., Middaugh, C.R., 2005. Silicone oil induced aggregation of proteins. J. Pharm. Sci. 94 (4), 918–927.

Katakam, M., Bell, L.N., Banga, A.K., 1995. Effect of surfactants on the physical stability of recombinant human hormone. J. Pharm. Sci. 84, 713–716.

Kiese, S., Papppenberger, A., Friess, W., Mahler, H.-C., 2008. Shaken, not stirred: mechanical stress testing, of an IgG1 antibody. J. Pharm. Sci. 97, 4347–4366.

Kishore, R.S.K., Kiese, S., Fischer, S., Pappenberger, A., Grauschopf, U., Mahler, H.-C., 2011. The degradation of polysorbates 20 and 80 and its potential impact on the stability of biotherapeutics. Pharm. Res. 28 (5), 1194–1210.

Lahloua, A., Blanchetb, B., Carvalhoa, M., Paula, M., Astier, A., 2009. Mechanically-induced aggregation of the monoclonal antibody cetuximab. Ann. Pharm. Fr. 67, 340–352.

Maa, Y.F., Hsu, S.S., 1997. Protein denaturation by combined effect of shear and air–liquid interface. Biotechnol. Bioeng. 54, 503–512.

Maa, Y.F., Hsu, S.S., 1996. Effect of high shear on proteins. Biotechnol. Bioeng. 51, 458–465.

Mahler, H.C., Müller, R., Frieβ, W., Delille, A., Matheus, S., 2005. Induction and analysis of aggregates in a liquid IgG1-antibody formulation. Eur. J. Pharm. Biopharm. 59, 407–417.

Martin, A.H., Cohen Stuart, M.A., Bos, M.A., Van Vliet, T., 2005. Correlation between mechanical behavior of protein films at the air/water interface and intrinsic stability of protein molecules. Langmuir 21 (9), 4083–4089.

Murray, B.S., Cattin, B., Schüler, E., Sonmez, Z.O., 2002. Response of adsorbed protein films to rapid expansion. Langmuir 18, 9476–9484.

Nielsen, L., Khurana, R., Coats, A., Frokjaer, S., Brange, J., Vyas, S., Uversky, V.N., Fink, A.L., 2001. Effect of environmental factors on the kinetics of insulin fibril formation: elucidation of the molecular mechanism. Biochemistry 40, 6036–6046.

Pantankar, S.V., 1983. Numerical Heat Transfer and Fluid Flow. Hemisphere Publishing Corp., Bristol, PA.

Patapoff, T.W., Esue, O., 2009. Polysorbate 20 prevents the precipitation of a monoclonal antibody during shear viscosity of monoclonal antibodies under shear. Pharm. Dev. Technol. 14, 659–664.

Patten, P.A., Schellekens, H., 2003. The immunogenicity of biopharmaceuticals. Lessons learned and consequences for protein drug development. Dev. Biol. (Basel) 112, 81–97.

Petkov, J.T., Gurkov, T.D., Campbell, B.E., Borwankar, R.P., 2000. Dilatational and shear elasticity of gel-like protein layers on air/water interface. Langmuir 16 (8), 3703–3711.

Ridout, M.J., Mackie, A.R., Wilde, P.J., 2004. Rheology of mixed β-casein/β-lactoglobulin films at the air–water interface. J. Agric. Food Chem. 52, 3930–3937.

Rosenberg, A., 2006. Effects of protein aggregates: an immunologic perspective. AAPS J. 8, 501–507.

Rosenberg, E., Hepbildikler, S., Kuhne, W., Winter, G., 2009. Ultrafiltration concentration of monoclonal antibody solutions: development of an optimized method minimizing aggregation. J. Membr. Sci. 342, 50–59.

Rougeot, C., Marchand, P., Dray, F., Job, J.C., Pierson, M., Ponte, C., Rochiccoili, P., Rappaport, R., 1991. Comparative study of biosynthetic human growth hormone immunogenicity in growth hormone deficient children. Horm. Res. 35, 76–81.

Schellekens, H., 2005. Factors influencing the immunogenicity of therapeutic proteins. Nephrol. Dial. Transplant. 20 (Suppl. 6), vi3–vi9.

Sicilian, J., 1990. A "FAVOR" based moving obstacle treatment for Flow-3D. Flow Science Technical Note #24.

Singh, J., Singh, S.P., Joneson, E., 2006. Measurement and analysis of US truck vibration for leaf spring and air ride suspensions, and development of tests to simulate these conditions. Pack. Tech. Sci. 19 (6), 309–323.

Song, X., Throckmorton, A., Wood, H., Antaki, J., Olsen, S., 2003. Computational fluid dynamics prediction of blood damage in a centrifugal pump. Artif. Organs 27, 938–941.

Tchobanoglous, G., Burton, F.L., Metcalf, Eddy, 2003. Wastewater Engineering: Treatment, Disposal and Reuse. McGraw-Hill, New York.

Thirumangalathu, R., Krishnan, S., Ricci, M.S., Brrms, N.D., Randolph, W.T., Carpenter, F.J., 2009. Silicone oil- and agitation-induced aggregation of a monoclonal antibody in aqueous solution. J. Pharm. Sci. 98, 3167–3181.

Thomas, C.R., Dunnill, P., 1979. Action of shear on enzymes-studies with catalase and urease. Biotechnol. Bioeng. 21, 2279–2302.

Thomas, C.R., Geer, D., 2011. Effects of shear on proteins in solution. Biotechnol. Lett. 33, 443–456.

Treuheit, M.J., Kosky, A.A., Brems, D.N., 2002. Inverse relationship of protein concentration and aggregation. Pharm. Res. 19, 511–516.

Tripp, B.C., Magda, J.J., Andrade, J.D., 1995. Adsorption of globular proteins at the ir/water interface as measured via dynamic surface tension: concentration dependence, mass-transfer considerations, and adsorption kinetics. J. Colloid Interface Sci. 173 (1), 16–27.

Tzannis, S.T., Hrushesky, W.J.M., Wood, P.A., Przybycien, T.M., 1997. Adsorption of a formulated protein on a drug delivery device suface. J. Colloid Interface Sci. 189 (2), 216–228.

Van Aken, G.A., Merks, M.T.E., 1996. Adsorption of soluble proteins to dilating surfaces. Colloids Surf. A 114, 221–226.

Van Reis, R., Zydney, A., 2007. Bioprocess membrane technology. J. Membr. Sci. 297, 16–50.

Virkar, P.D., Narendaranathan, T.J., Hoare, M., Dunnill, P., 1981. Studies of the effects of shear on globular-proteins-extension of high shear fields and to pumps. Biotechnol. Bioeng. 23, 425–429.

Wang, W., 1999. Instability, stabilization, and formulation of liquid protein pharmaceuticals. Int. J. Pharm. 185, 129–188.

Wang, W., Wang, Y.J., Wang, D.Q., 2008. Dual effects of Tween 80 on protein stability. Int. J. Pharm. 347, 31–38.

Wei, G., 2005. A fixed-mesh method for general moving objects. Flow Science Technical Note #73.